REPORT ONR-CR215-263-1

ADA087134

(12)

LEVEL II

OFFICE OF NAVAL RESEARCH

USN ONR

BASIC STUDIES OF WING-BODY INTERFERENCE
AT HIGH ANGLES OF ATTACK AND
SUPERSONIC SPEEDS

Goetz H. Klopfer
and Jack N. Nielsen

Contract No. N00014-78-C-0490
ONR Task 215-263

October 1979

Final Report

Approved for public release; distribution unlimited

DTIC
ELECTE
JUL 24 1980

S   D

B

PREPARED FOR THE
OFFICE OF NAVAL RESEARCH • 800 N. QUINCY ST. • ARLINGTON, VA. 22217

80 7 21 014

COPY NO. 17

REPORT DOCUMENTATION PAGE		READ INSTRUCTIONS BEFORE COMPLETING FORM
1. REPORT NUMBER ONR CR-215-263-1	2. GOVT ACCESSION NO. AD-A087 134	3. RECIPIENT'S CATALOG NUMBER
4. TITLE (and Subtitle) BASIC STUDIES OF WING-BODY INTERFERENCE AT HIGH ANGLES OF ATTACK AND SUPERSONIC SPEEDS.		5. TYPE OF REPORT & PERIOD COVERED Final Report. 6/1/78 - 5/31/79
		6. PERFORMING ORG. REPORT NUMBER NEAR-TR-206
7. AUTHOR(s) Goetz H. Klopfer and Jack N. Nielsen		8. CONTRACT OR GRANT NUMBER(s) N00014-78-C-0490
9. PERFORMING ORGANIZATION NAME AND ADDRESS Nielsen Engineering & Research, Inc. 510 Clyde Avenue Mountain View, CA 94043		10. PROGRAM ELEMENT, PROJECT, TASK AREA & WORK UNIT NUMBERS 61153N-14 RR0141184 NR215-263
11. CONTROLLING OFFICE NAME AND ADDRESS Office of Naval Research Arlington, Virginia 22217		12. REPORT DATE October 1979
		13. NUMBER OF PAGES
14. MONITORING AGENCY NAME & ADDRESS(if different from Controlling Office)		15. SECURITY CLASS. (of this report) Unclassified
		15a. DECLASSIFICATION/DOWNGRADING SCHEDULE

16. DISTRIBUTION STATEMENT (of this Report)

Approved for public release, distribution unlimited

17. DISTRIBUTION STATEMENT (of the abstract entered in Block 20, if different from Report)

18. SUPPLEMENTARY NOTES

19. KEY WORDS (Continue on reverse side if necessary and identify by block number)

Numerical Analysis   Wing-Body Interference
Supersonic Flows   High Angle of Attack Aerodynamics
Euler Equations
Conical Flows

20. ABSTRACT (Continue on reverse side if necessary and identify by block number)
    The problem of computing the steady inviscid supersonic flows about thin wings having sharp subsonic leading edges and leading-edge separation is solved in this paper. Both wings alone or wings in the presence of the body are considered.

    To obtain an efficient procedure the steady Euler equations are used as the basic governing equations as opposed to the more complicated Navier-Stokes equation. The viscous effects,

DD FORM 1473   EDITION OF 1 NOV 65 IS OBSOLETE
1 JAN 73

Block 20 (continued)

important near the sharp leading edges, are simulated by a
Kutta condition applied at the leading edges of the wings.
The rest of the flow field is essentially controlled by the
inviscid equations. The equations, written in conservation
form in generalized curvilinear coordinates, are approximated
by MacCormack's second-order accurate predictor-corrector
algorithm. The flow tangency conditions at the body surface
are satisfied by Abbett's scheme and the outer bow-shock
position by the Rankine-Hugoniot jump relations. Internal
shock waves or tangentially discontinuities are captured.
The slip surface emanating from the leading edge of the
sharp wing excited nonlinear instabilities in the MacCormack's
scheme, which were stabilized by special flow dependent
fourth-order damping terms.

Comparisons have been made between predicted pressure
distributions and measured pressure distribution for an $R = 1$
delta wing at $\alpha = 10°$ at $M_\infty = 3.0$. Good agreement is obtained.
A solution was also obtained for the same wing mounted on a
body of revolution at the same angle of attack and Mach number.
Large losses of favorable wing-body interference were predicted
which are in good agreement with experiment.

SUMMARY

     This paper addresses the problem of computing the steady
inviscid supersonic flows about thin wings having sharp sub-
sonic leading edges and leading-edge separation. For such
wings the flow on the suction side tends to spiral into a vor-
tex. Both wings alone or wings in the presence of the body are
considered.

     Previous analytical studies to solve these flow fields
have used the leading-edge suction analogy, linear slender-wing
theory, or detached flow methods. These studies are basically
inviscid. Viscous effects have been included by Vigneron,
et al. in a numerical study of supersonic flows over delta
wings with sharp subsonic leading edges using the Navier-
Stokes equations. To obtain a more efficient procedure than
Vigneron's et al., we use the steady Euler equations as the
basic governing equations as opposed to the more complicated
Navier-Stokes equation. The viscous effects, important near
the sharp leading edges, are simulated by a Kutta condition
applied at the leading edges of the wings. The rest of the
flow field is essentially controlled by the inviscid equations.
The equations are written in conservation form in generalized
curvilinear coordinates. The equations are approximated by
MacCormack's second-order accurate predictor-corrector
algorithm. The flow tangency conditions at the body surface
are satisfied by Abbett's scheme and the outer bow-shock
position by the Rankine-Hugoniot jump relations. Any internal
shock waves or tangentially discontinuities are captured by the
scheme. It was found that the slip surface emanating from the
leading edge of the sharp wing excited nonlinear instabilities
in the MacCormack's scheme. The addition of special flow
dependent fourth-order damping terms stabilized the scheme.

1

Comparisons have been made between predicted pressure distributions and measured pressure distribution for an $R=1$ delta wing at $\alpha = 10°$ at $M_\infty = 3.0$. Good agreement is obtained. A solution was also obtained for the same wing mounted on a body of revolution at the same angle of attack and Mach number. Large losses of favorable wing-body interference were predicted which are in good agreement with experiment.

ACKNOWLEDGMENT

ACCESSION for		
NTIS	White Section	✓
DDC	Buff Section	☐
UNANNOUNCED		☐
JUSTIFICATION		
BY		
DISTRIBUTION/AVAILABILITY CODES		
Dist.	AVAIL. and/or	SPECIAL
A		

TABLE OF CONTENTS

1. INTRODUCTION AND BACKGROUND

As a result of past work (ref. 1) done at Nielsen Engineering & Research, Inc. (NEAR) for the Office of Naval Research (ONR) to produce engineering prediction methods for missiles up to angle of attack of 50° and Mach numbers up to 3.0, several important problems in high angle of attack aero- dynamics have emerged. It is the purpose of this report to describe these problems and to attempt their solution using the Euler equations. While these problems have arisen in connection with missile aerodynamics, they are equally impor- tant for airplanes.

The present work is a logical extension of the work NEAR has carried out for ONR over the past four years. During the first two years, paneling (inviscid) methods together with vortex theory were used to develop pressure predictive tech- niques for complete missiles at supersonic speeds and angles of attack to 20°. In the third and fourth years engineering methods were developed to predict forces and moments acting on canard cruciform missile to 50° angle of attack. These methods, based on data base and rational modeling, produced useful methods of reasonable accuracy, but also uncovered important aerodynamic effects which need more study in their own right. In order to extend the range of the engineering design codes and to improve the rational modeling approach, it is necessary to undertake further work. It is believed that such work should utilize recent advances in viscous and inviscid numerical computation techniques supplemented by further experimental work.

Two of the major problems which have been uncovered are the adverse effect of wing-body interference on wing lift at high angles of attack and the special behavior of body vortices

at supercritical crossflow Mach numbers. This report addresses
the first problem only.

On a wing-body combination at subsonic and moderately
supersonic speed, the effect of the body on the wing is to
increase the wing lift so long as the angle of attack is small.
As an example, consider the upwash in a crossflow plane normal
to the body. As it goes around the body, the air speeds up and
produces an angle of attack equal to 2α at the side of the body.
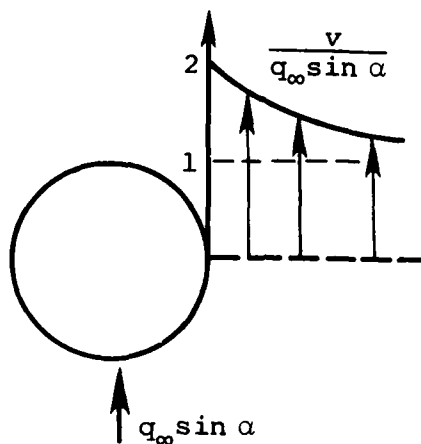
Putting the wing panels in this field causes an increased lift
over what they would develop if the panels were made into a
wing at angle of attack α. The wing-body interference factor
K_W is a measure of this interference.

$$K_W = \frac{\text{Lift of wing panel attached to fuselage (at } \alpha)}{\text{Lift of wing panel in wing alone (at } \alpha)}$$

According to potential flow theory, K_W runs from 1 for no
fuselage up to 2 for a small fin on a large fuselage (ref. 2).

In the previous work, we have determined K_W from experi-
mental data for a series of wings and Mach numbers up to 45°
angle of attack. Figure 1 shows these experimental results
for a delta fin of aspect ratio 1 mounted on a body whose

8

diameter is one-half the total span of the wing-body. As the angle of attack is increased, the value of K_W decreases sharply, indicating less favorable interference of the body on the wing. At high Mach numbers the adverse interference is substantially increased.

It is of interest to examine the environment in which a fin or wing might operate at high angles of attack. We are in a position to calculate the inviscid flow in which such a fin or wing might operate using a computer program (refs. 3 and 4) for solving the Euler equations developed at NASA/Ames Research Center. Figure 2 shows such a flow for a supersonic crossflow Mach number with the computer program operating in the shock-capturing mode. Within the bow shock from the nose of the body, the flow in the crossflow plane is mostly subsonic. However there are embedded supersonic flow regions bounded by $M = 1$ lines and crossflow shocks. The flow as shown represents an inviscid flow with rotation caused by the bow shock curvature. The vortical singularity line exhibited by the flow is characteristic of such solutions. In the real fluid case, the wake of the body will modify the flow and may eliminate the "vortical singularity".

It is clear that inserting a fin in the body flow which is shown in figure 2 can cause significant changes in the fin aerodynamic force and moment over what they would be for low-speed crossflow past the body. In fact this altered flow field accounts in the main for the considerable reduction in K_W for this condition as shown by figure 1.

This report addresses the problem of computing the steady inviscid supersonic flows about wings having subsonic leading edges with leading-edge separation. For such wings the flow on the suction side tends to spiral into a vortex above the wing. This vortex provides for lift augmentation at low supersonic speeds. Previous analytical studies to solve these flow fields

9

have used the leading-edge suction analogy, linear slender-wing theory, or detached flow methods (ref. 5). These studies are basically inviscid. Viscous effects have been included by Vigneron, et al. (ref. 6) in a numerical study of supersonic flows over delta wings with sharp subsonic leading edges using the Navier-Stokes equations.

Here we wish to calculate flows around wings and wing-body combinations with sharp leading edges. To obtain a more efficient procedure than Vigneron's et al., we use the inviscid steady Euler equations as the basic governing equations as opposed to the more complicated Navier-Stokes equation. The viscous effects, important near the sharp leading edges, are simulated by a Kutta condition applied at the leading edges of the wings. The rest of the flow field is essentially controlled by the inviscid equations. To further simplify the calculations, we consider cases for which the axial Mach number is supersonic.

A brief outline of the general approach of studying the wing-body interference problem for steady supersonic flows is now given.

The steady Euler equations are written in conservation form in generalized curvilinear coordinates. The general coordinate system is fitted between the body and the outer bow shock. The coordinate system is fitted to the body by a conformal transformation which transforms the wing-body or wing alone to a unit circle. To fit the outer shock to the coordinate system, the radial distance is normalized with respect to the distance between the outer shock and the body. A typical mesh is shown in figures 3(a) and (b) for the planar delta wing. The equations are approximated by MacCormack's second-order accurate predictor-corrector algorithm (refs. 3 and 4). The flow tangency conditions at the body surface are satisfied by Abbett's scheme (ref. 7) and the outer bow-shock position by the Rankine-Hugoniot jump relations. Any internal shock waves

10

or tangentially discontinuities are captured by the scheme. It
was found that the slip surface emanating from the leading edge
of the sharp wing excited nonlinear instabilities in the
MacCormack's scheme. The addition of special flow dependent
fourth-order damping terms stabilized the scheme.

Because of the singularity of the conformal transformation,
the transformed Euler equations become indeterminate as the wing
tip is approached. A separate specification of the primitive
flow variables at the wing tip is required. This is done by
satisfying the Kutta condition, that is, the flow at the wing
tip is tangent to the wing surface. The pressure, entropy, and
flow direction (in the plane of the wing) are obtained by
averaging the values obtained numerically just above and below
the wing tip. Constant total enthalpy completes the specifica-
tion of the wing tip flow variables. For the wing-alone
results, no wing thickness is used. The singularity of the
transformation at the wing-body juncture is avoided by moving
a distance ε off the unit circle.

In the following four sections, the governing transformed
equations, the body geometry, the numerical scheme and the
boundary and initial conditions are described. The numerical
results are presented and discussed in the sixth section. In
the seventh section conclusions and recommendations are made.
The final section, an appendix, describes briefly the graphics
required to obtain the crossflow particle trajectories and the
conical streamlines.

2. STEADY EULER EQUATIONS

The conservation-law form of the fluid dynamic equation
for steady, inviscid, three-dimensional compressible flow of
an ideal gas (steady Euler equations) in Cartesian form are

11

$$\frac{\partial \hat{E}}{\partial x} + \frac{\partial \hat{F}}{\partial y} + \frac{\partial \hat{G}}{\partial z} = 0 \qquad (1)$$

where $\hat{E}$, $\hat{F}$, and $\hat{G}$ are defined as

$$\hat{E} = \begin{bmatrix} \rho u \\ \rho u^2 + kp \\ \rho uv \\ \rho uw \end{bmatrix} \qquad \hat{F} = \begin{bmatrix} \rho u \\ \rho uv \\ \rho v^2 + kp \\ \rho vw \end{bmatrix} \qquad \hat{G} = \begin{bmatrix} \rho w \\ \rho uw \\ \rho vw \\ \rho w^2 + pk \end{bmatrix}$$

Equation (1) represents the conservation of mass and momentum. The pressure and density are normalized with respect to the stagnation conditions and the Cartesian velocity components (u,v,w) with respect to the maximum adiabatic velocity where $k = 2\gamma/(\gamma-1)$ and γ is the ratio of the specific heats. The system of equations is closed by the integrated form of the steady energy equation which in nondimensional form is

$$p = \rho(1 - u^2 - v^2 - w^2) \qquad (2)$$

For a given free-stream Mach number and angle of attack α, the remaining free-stream variables in nondimensional form are given by

$$p_\infty = \{1 + [(\gamma-1)/2]M_\infty^2\}^{-\gamma/(\gamma-1)}$$

$$\rho_\infty = \{1 + [(\gamma-1)/2]M_\infty^2\}^{-1/(\gamma-1)}$$

$$u_\infty = 0$$

$$v_\infty = q_\infty \sin \alpha$$

$$w_\infty = q_\infty \cos \alpha$$

where

$$q_\infty = (u_\infty^2 + v_\infty^2 + w_\infty^2)^{1/2} = \left[\frac{\frac{\gamma-1}{2} M_\infty^2}{1 + \frac{\gamma-1}{2} M_\infty^2} \right]^{1/2}$$

To obtain a surface-oriented coordinate system, the system (1) is transformed from the Cartesian space (x,y,z) into another arbitrary curvilinear system (z,r,ϕ) where $r = 1$ defines the body surface. The general transformation is (the particular transformations considered are given in section 3)

$$z = z$$
$$r = r(x,y,z) \qquad\qquad (3)$$
$$\phi = \phi(x,y,z)$$

The transformed equation, obtained by Viviand's (ref. 8) procedure, are in slightly rearranged form

$$\frac{\partial}{\partial z} \tilde{E} + \frac{\partial}{\partial r} \tilde{F} + \frac{\partial}{\partial \phi} \tilde{G} = 0 \qquad\qquad (4)$$

where

$$\tilde{E} = \frac{1}{J} \begin{bmatrix} \rho U \\ \rho w U + pk \\ \rho v U \\ \rho u U \end{bmatrix} ; \quad \tilde{F} = \frac{1}{J} \begin{bmatrix} \rho V \\ \rho w V + r_z pk \\ \rho v V + r_y pk \\ \rho u V + r_x pk \end{bmatrix} ; \quad \tilde{G} = \frac{1}{J} \begin{bmatrix} \rho W \\ \rho w W + \phi_z pk \\ \rho v W + \phi_y pk \\ \rho u W + \phi_x pk \end{bmatrix}$$

and

$$U = w$$
$$V = r_x u + r_y v + r_z w \qquad\qquad (5)$$
$$W = \phi_x u + \phi_y v + \phi_z w$$

13

where U, V, and W are the contravariant velocities written without the metric normalization. The metric terms are obtained from the chain rule expansion of x_r, y_r, etc. and solved for r_x, r_y, etc. to give

$$
\begin{aligned}
z_x &= 0 & r_x &= Jy_\phi & \phi_x &= -Jy_r \\
z_y &= 0 & r_y &= -Jx_\phi & \phi_y &= Jx_r \\
z_z &= 1 & r_z &= J(y_z x_\phi - x_z y_\phi) & \phi_z &= J(x_z y_r - x_r y_z)
\end{aligned}
\tag{6}
$$

and

$$
J^{-1} = x_r y_\phi - x_\phi y_r
$$

where J is the Jacobian of the transformation from the arbitrary curvilinear space (z, r, ϕ) to the Cartesian space (x, y, z), figure 4. It should be pointed out that both coordinate systems are left-handed, the reason being that the parent code (refs. 3 and 4) used for this study was written for a left-handed system.

To fit the outer bow shock wave, the outer mesh boundary must coincide with the bow shock. Since this bow shock is a variable three-dimensional surface it is necessary to introduce another transformation which normalizes the distance between the body boundary and the bow shock surface. The location of the bow shock surface is determined by the Rankine-Hugoniot conditions during the course of the numerical computation described in a later section. At the same time it is desirable to have arbitrary clustering functions in the transformation so that mesh points can be concentrated near the body surface, wing tip, or wing-body juncture for increased resolution in areas of rapid changes of the flow variables or the previously mentioned transformation metrics.

The equations of the independent variable transformation are

$$\zeta = z$$
$$\tau = h(\xi) \tag{7}$$
$$\eta = f(\phi)$$

where h and f are clustering functions

$$\xi = (r - r_b)/(r_s - r_b)$$

$r_b = r_b(z, \phi)$, the body surface radius

and

$r_s = r_s(z, \phi)$, the outer shock radius

to be determined as part of the numerical solution procedure. The derivatives are

$$\frac{\partial}{\partial z} = \frac{\partial}{\partial \zeta} + \tau_\xi \xi_z \frac{\partial}{\partial \tau}$$

$$\frac{\partial}{\partial r} = \tau_\xi \xi_r \frac{\partial}{\partial \tau} \tag{8}$$

$$\frac{\partial}{\partial \phi} = \tau_\xi \xi_\phi \frac{\partial}{\partial \tau} + \eta_\phi \frac{\partial}{\partial \eta}$$

The system (1) is now in weakly conservative form (i.e. no longer strongly conservative in the spirit of Viviand)

$$\frac{\partial}{\partial \zeta} E + \frac{\partial}{\partial \tau} F + \frac{\partial}{\partial \eta} G + H = 0 \tag{9}$$

where

$$E = \tilde{E}$$
$$F = \tau_\xi \{\xi_z \tilde{E} + \xi_r \tilde{F} + \xi_\phi \tilde{G}\}$$
$$G = \eta_\phi \tilde{G}$$

15

and

$$H = -\frac{\tau_{\xi\xi}}{\tau_\xi} \{\xi_z \tilde{E} + \xi_r \tilde{F} + \xi_\phi \tilde{G}\} - \frac{1}{\xi_r} \{\xi_{zr} \tilde{E} + \xi_{\phi r} \tilde{G}\}$$
$$- \frac{\eta_{\phi\phi}}{\eta_\phi} \tilde{G}$$

We also have

$$\tau_\xi = \frac{dh(\xi)}{d\xi}, \quad \tau_{\xi\xi} = \frac{d^2 h(\xi)}{d\xi^2}$$

$$\xi_r = 1/(r_s - r_b)$$

$$\xi_z = -\{r_{bz} + \xi(r_{sz} - r_{bz})\} \cdot \xi_r \tag{10}$$

$$\xi_\phi = -\{r_{b\phi} + \xi(r_{s\phi} - r_{b\phi})\} \cdot \xi_r$$

$$\eta_\phi = \frac{df(\phi)}{d\phi} \quad \text{and} \quad \eta_{\phi\phi} = \frac{d^2 f(\phi)}{d\phi^2}$$

The functions h and f are the clustering transformations in the r and ϕ directions, respectively. The normalization between the body surface and the shock is given by the variable ξ.

The equation is no longer in strongly conservative form (i.e. $H \equiv 0$) to simplify the decoding of the dependent E vector. The finite difference form of eq. (9) is integrated with respect to the hyperbolic coordinate ζ to yield values of E. The physical flow variables p, ρ, u, v, w must be decoded from the components e_i of E. Explicit expressions are possible for the physical flow variables if the system is weakly conservative.

This is not possible in the strongly conservative form since the E vector would have a form similar to F in eq. (9).

The physical flow variables are obtained by the solution of five simultaneous nonlinear equations consisting of the four components e_i and the integrated energy equation (eq. (2)). The velocity components u and v are given by

$$u = e_4/e_1$$
$$v = e_3/e_1$$

(11)

The e_i along with eqs. (11) and the Jacobian are used to obtain an implicit relation in w from eq. (2).

$$(1-k)w^2 - \frac{e_2}{e_1} w + k\left(1 - \frac{e_3^2 + e_4^2}{e_1^2}\right) = 0$$

(12)

The decoding procedure is reduced to finding the roots of the quadratic eq. (12). Two roots exists corresponding to a subsonic and a supersonic flow in the z-direction. The root corresponding to supersonic flow is the desired solution.

$$w = \frac{1}{2e_1(1-k)} \left[e_2 + \{e_2^2 - 4(1-k)k(e_1^2 - e_3^2 - e_4^2)\}^{1/2} \right]$$

(13)

The density is obtained from

$$\rho = e_1 \cdot J/w$$

(14)

and the pressure from eq. (2).

This decoding procedure gives explicit expressions for the physical flow variables. For the strongly conservative form of the governing equations a Newton-Raphson procedure is necessary to determine the flow variables. The additional

computing time was not thought to be worthwhile simply to
maintain the strongly conservative form. Apparently the cor-
rect jump conditions are still obtained with the equations in
weakly conservative form (ref. 3).

3. BODY GEOMETRY

In this study two types of body geometries are considered:
a planar wing alone and a planar mid-wing on a cylindrical body.
The latter configuration is shown in figure 4. The wing lies
in the x-z plane. Both the body radius and wing semispan are
arbitrary functions of the axial coordinate z. By a conformal
transformation the wing-body configuration is transformed into
a cylinder of unit radius. The transformation is given more
conveniently in the terms of the transformed space variables
(z, r, ϕ). The mapping between the transformed space and the
physical space (x, y, z) is given by

$$g = \frac{R}{4} \left\{ Z + \frac{1}{Z} \pm \sqrt{(Z + \frac{1}{Z})^2 - 16B^2/R^2} \right\} \qquad (15)$$

$$z = z$$

where

$$g = x + iy$$

$$i = \sqrt{-1}$$

$$R = R_w(z) = B^2(z)/R_w(z) \qquad R_w \geq B$$

$$Z = re^{i(\phi - \pi/2)} = re^{i\theta}$$

and the positive (negative) sign in front of radical applies
to the upper (lower) half plane.

This single transformation covers all the configurations
considered in this report. Circular bodies alone, planar wings

18

alone, and planar mid-wing, circular-body combinations are ob-
tained simply by setting $R_w = B$, $B = 0$, and $R_w > B$, respectively.

The transformation metrics are easily obtainable by dif-
ferentiation of the above mapping.

$$\frac{\partial g}{\partial z} = g \frac{R'}{R} \pm \frac{4 \frac{B^2}{R^2} R' - \frac{B}{R} B'}{\sqrt{(Z + \frac{1}{Z})^2 - 16B^2/R^2}}$$

$$\frac{\partial g}{\partial r} = \frac{R}{4r}(Z - \frac{1}{Z})\left\{1 \pm \frac{Z + \frac{1}{Z}}{\sqrt{(Z + \frac{1}{Z})^2 - 16B^2/R^2}}\right\} \qquad (16)$$

$$\frac{\partial g}{\partial \phi} = \frac{iR}{4}(Z - \frac{1}{Z})\left\{1 \pm \frac{Z + \frac{1}{Z}}{\sqrt{(Z + \frac{1}{Z})^2 - 16B^2/R^2}}\right\}$$

Separating real and imaginary parts of g_z, g_r, and g_ϕ obtains

$$x_z, y_z, \quad x_r, y_r, \quad \text{and } x_\phi, y_\phi, \quad \text{respectively}$$

Substituting these into eq. (6) obtains the requisite metrics
for eq. (4).

The transformation is well behaved (i.e. $J^{-1} \neq 0$ or $\neq \infty$)
everywhere except at the wing tip and at the wing-body juncture.
At the wing tip all the metrics and the Jacobian vanish, leav-
ing eq. (4) indeterminate. This requires special procedures at
the wing tip as discussed in section 5. At the wing-body
juncture, the inverse of the radical of eqs. (16) becomes
infinite. This singular behavior is due to the abrupt jump of

the surface slope between the body and wing. If the analytic expressions (eq. (16)) for the metrics are replaced by their finite difference equivalent, the singularity is automatically avoided and no special treatment is required at these points. However a different procedure is used here as described in section 5.E.

4. FINITE DIFFERENCE EQUATION

The flow equations, eq. (9), are approximated by MacCormack's second-order, predictor-corrector scheme. Since the outer bow shock wave is fitted and the internal shock waves or tangential discontinuities are captured, it is essential that an efficient numerical scheme be used. Kutler has found (ref. 9) MacCormack's scheme to be one of the most efficient and easily implementable schemes available.

The numerical algorithm can be written for the field points $(4 \leq j \leq NT2-1; \ 3 \leq k \leq NPHI$, see fig. 5) as

$$\overline{E_{j,k}^{n+1}} = E_{j,k}^n - \frac{\Delta \zeta^{n+1}}{\Delta \tau} (F_{j+1,k}^n - F_{j,k}^n) - \frac{\Delta \zeta^{n+1}}{\Delta \eta} (G_{j,KPL}^n - G_{j,KPR}^n)$$

$$- \Delta \zeta^{n+1} H_{j,k}^n + \Delta E_{j,k}^n \Big|_m + \Delta E_{j,k}^n \Big|_r \tag{17a}$$

for the predictor step and as

$$E_{j,k}^{n+1} = \frac{1}{2} \left[E_{j,k}^n + \overline{E_{j,k}^{n+1}} - \frac{\Delta \zeta^{n+1}}{\Delta \tau} (\overline{F_{j,k}^{n+1}} - \overline{F_{j-1,k}^{n+1}}) \right.$$

$$\left. - \frac{\Delta \zeta^{n+1}}{\Delta \eta} (\overline{G_{j,KCL}^{n+1}} - \overline{G_{j,KCR}^{n+1}}) - \Delta \zeta^{n+1} \overline{H_{j,k}^{n+1}} \right]$$

$$+ \Delta E_{j,k}^{n+1} \Big|_m + \Delta E_{j,k}^{n+1} \Big|_r \tag{17b}$$

20

for the corrector step, where

$$KPL = k + NFLIP$$

$$KPR = k - 1 + NFLIP$$

$$KCL = k + 1 - NFLIP$$

$$KCR = k - NFLIP$$

$$E^n_{j,k} = E(\zeta^n, j\Delta\tau, k\Delta\eta)$$

$$F^n_{j,k} = F(E^n_{j,k}, \zeta^n, j\Delta\tau, k\Delta\eta)$$

$$F^{\overline{n+1}}_{j,k} = F(E^{\overline{n+1}}_{j,k}, \zeta^n + \Delta\zeta^{n+1}, j\Delta\tau, k\Delta\eta)$$

and

$$\zeta^n = \zeta_o + \sum_{\ell=1}^{n} \Delta\zeta^\ell$$

The value of NFLIP alternates cyclically between one and zero with the integration steps to obtain unbiased results. The increments $\Delta\tau$ and $\Delta\eta$ are the mesh spacings in the radial and meridional directions and, $\Delta\zeta^n$ is the marching step size between the n-1 and nth computational planes. The terms $\Delta E^n_{j,k}|_{m,r}$ and $\Delta E^{\overline{n+1}}_{j,k}|_{m,r}$ are fourth-order damping terms introduced to control the severe nonlinear instabilities experienced near the leading edge of the wing. The damping terms are given by

$$\Delta E^L_{j,k}\bigg|_m = \mu^L_m \left(\frac{E_{j,k+1} \cdot J_{j,k+1} - 2E_{j,k} \cdot J_{j,k} + E_{j,k-1} \cdot J_{j,k-1}}{J_{j,k}} \right)$$

$$(18a)$$

$$\Delta E^L_{j,k}\bigg|_r = \mu^L_r \left(\frac{E_{j+1,k} \cdot J_{j+1,k} - 2E_{j,k} \cdot J_{j,k} + E_{j-1,k} \cdot J_{j-1,k}}{J_{j,k}} \right)$$

$$(18b)$$

where

$$\mu_m^L = \frac{C_m}{2} \frac{\left| \rho_{j,k+\ell+1} - 2\rho_{j,k+\ell} + \rho_{j,k+\ell-1} \right|}{\left| \rho_{j,k+\ell+1} + 2\rho_{j,k+\ell} + \rho_{j,k+\ell-1} \right|}$$

and

$$\mu_r^L = \frac{C_r}{2} \frac{\left| \rho_{jj+1,k} - 2\rho_{jj,k} + \rho_{jj-1,k} \right|}{\left| \rho_{jj+1,k} + 2\rho_{jj,k} + \rho_{jj-1,k} \right|}$$

where $L = n$ or $\overline{n+1}$, $\ell = 0$ or $1-2\cdot$NFLIP, and $jj = j$ or $j+1$, depending on whether the damping terms apply for the predictor step, eq. (17a), or the corrector step, eq. (17b). These damping terms are similar to those used by Baldwin and MacCormack (ref. 11). The pressure terms that they originally used have here been replaced with the densities. It was found that the tangential discontinuity emanating from the leading edge of the wing forced large oscillations in the densities and very little in the pressures. Thus the original damping did not adequately control the nonlinear instability near the wing leading edges. The arbitrary coefficients C_r and C_m range from 0 for no damping to 1 for the maximum allowable damping. Typical values were $C_r = 0.1$ and $C_m = 0.5$, for the radial and meridional damping, respectively.

The above finite-difference equations are applied only to the field points. At the body ($j = 3$, $3 \le k \le$ NPHI) Abbett's scheme is used to satisfy surface tangency as discussed later. It requires information provided by the finite difference algorithm. The algorithm used for the field points, however, cannot be used on the surface since it requires points on both sides of the point being advanced and thus data at a set of points that would lie inside the body. Therefore, a second-order accurate algorithm is used requiring data only on or

outside the body. This scheme uses the predictor step of
MacCormack's method, eq. (17a), without the fourth-order damping
terms, followed by the corrector step given by

$$
\begin{aligned}
E_{j,k}^{n+1} = \frac{1}{2}\Bigg[& E_{j,k}^{n} + E_{j,k}^{\overline{n+1}} - \frac{\Delta\zeta^{n+1}}{\Delta\tau}\left(F_{j+1,k}^{\overline{n+1}} - F_{j,k}^{\overline{n+1}}\right) \\
& - \frac{\Delta\zeta^{n+1}}{\Delta\eta}\left(G_{j,KCL}^{\overline{n+1}} - G_{j,KCR}^{\overline{n+1}}\right) - \Delta\zeta^{n+1}\, H_{j,k}^{\overline{n+1}} \\
& + \frac{\Delta\zeta^{n+1}}{\Delta\tau}\left(F_{j+2,k}^{n} - 2F_{j+1,k}^{n} + F_{j,k}^{n}\right)\Bigg]
\end{aligned}
\tag{19}
$$

where $j = 3$. After MacCormack's predictor and eq. (19) have
been used to advance the data at the body, Abbett's scheme is
used as a final corrector. This scheme is described in a later
section.

At the shock wave, a predictor-corrector sequence is
again used and requires data at the shock and one point below
it. The algorithm is as follows:

Predictor:

$$
\begin{aligned}
E_{j,k}^{n+1} = E_{j,k}^{n} & - \frac{\Delta\zeta^{n+1}}{\Delta\tau}\left(F_{j,k}^{n} - F_{j-1,k}^{n}\right) \\
& - \frac{\Delta\zeta^{n+1}}{\Delta\eta}\left(G_{j,KPL}^{n} - G_{j,KPR}\right) - \Delta\zeta^{n+1}\, H_{j,k}^{n}
\end{aligned}
\tag{20a}
$$

Corrector:

$$
\begin{aligned}
E_{j,k}^{n+1} = \frac{1}{2}\Bigg[& E_{j,k}^{n} + E_{j,k}^{n+1} - \frac{\Delta\zeta^{n+1}}{\Delta\tau}\left(F_{j,k}^{\overline{n+1}} - F_{j-1,k}^{\overline{n+1}}\right) \\
& - \frac{\Delta\zeta^{n+1}}{\Delta\eta}\left(G_{j,KCL}^{\overline{n+1}} - G_{j,KCR}^{\overline{n+1}}\right) - \Delta\zeta^{n+1}\, H_{j,k}^{\overline{n+1}}\Bigg]
\end{aligned}
\tag{20b}
$$

where $j = NT2$. Equations (20a) and (20b) are used in conjunc-
tion with the Rankine-Hugoniot relations, described later, to
determine the peripheral shock shape. It should be noted that

the damping terms are not used for the boundary finite-difference equations.

The integration stepsize is determined by the stability bound of the numerical scheme. The stepsize must be small enough to satisfy the stability requirement of the scheme but large enough to finish the computation with a minimum of time. The use of the largest possible stepsize for hyperbolic equations insures that the finite-difference scheme is as nearly compatible with the method of characteristics as possible. The bound on the stepsize value is obtained by the amplification matrix theory. This method is based on a locally linear (frozen coefficient) analysis of the governing partial differential equations coupled with a discrete harmonic analysis of the linear difference scheme. The partial differential equation system, eq. (9), is rewritten in primitive variable, nonconservative form as

$$\frac{\partial U}{\partial \zeta} + M \frac{\partial U}{\partial \tau} + N \frac{\partial U}{\partial \eta} + H = 0 \tag{21}$$

where $U = (u,v,w,p,\rho)^T$, and M and N are the coefficient matrices given below. The amplification matrix theory for the two-dimensional ζ, τ space requires that

$$\frac{\Delta \zeta}{\Delta \tau} \leq 1/(\sigma_M)_{max} \tag{22}$$

and

$$(\sigma_M) = |\sigma(M)|_{local\ max}$$

where σ_M is the local maximum modulus of the eigenvalues of the matrix M for a given grid point in the field. The maximum of the local maximum of the eigenvalues in a particular ζ = constant plane is what is needed in the above equation. A similar condition is obtained in the z, η space

$$\frac{\Delta \zeta}{\Delta \eta} \leq 1/(\sigma_N)_{max}; \quad \sigma_N = |\sigma(N)|_{local\ max} \tag{23}$$

24

This planar analysis has been shown to give a good bound on the stepsize in multidimensional problems if eqs. (22) and (23) are replaced by

$$\frac{\Delta \zeta}{\Delta \tau} = CFL/(\sigma_M)_{max} \tag{24a}$$

$$\frac{\Delta \zeta}{\Delta \eta} = CFL/(\sigma_N)_{max} \tag{24b}$$

where CFL is the Courant-Friedricks-Lewy number. The CFL number < 1 can be varied during the computation and is usually assigned a value of 0.9 or less. When applying eq. (24) to determine $\Delta \zeta$, the mesh spacing $\Delta \tau$ and $\Delta \eta$ are given. It is therefore necessary to determine the minimum $\Delta \zeta$ predicted by the two relations. This minimum $\Delta \zeta$, which is recalculated after every few (typically five or less) integration steps, is the one used for the succeeding steps in the integration procedure.

The values σ_M and σ_N required in eq. (24) are determined from the matrices M and N. The coefficient matrix M is given by

$$M = \frac{\partial \tau}{\partial z} I + \frac{\partial \tau}{\partial r} (A^{-1}B) + \frac{\partial \tau}{\partial \phi} (A^{-1}C) \tag{25a}$$

and N is given by

$$N = \frac{\partial \eta}{\partial \phi} (A^{-1}C) \tag{25b}$$

where I is the identity matrix and $(A^{-1}B)$ is given by

$$(A^{-1}B) = \begin{bmatrix} \dfrac{UV-r_z a^2}{U^2-a^2} & \dfrac{-r_y a^2}{U^2-a^2} & \dfrac{-r_x a^2}{U^2-a^2} & \dfrac{k(r_z U-V)}{\rho(U^2-a^2)} & 0 \\[3ex] 0 & \dfrac{V}{U} & 0 & \dfrac{r_y k}{\rho U} & 0 \\[3ex] 0 & 0 & \dfrac{V}{U} & \dfrac{r_x k}{\rho U} & 0 \\[3ex] \dfrac{a^2 \rho(r_z U-V)}{k(U^2-a^2)} & \dfrac{a^2 \rho r_y U}{k(U^2-a^2)} & \dfrac{a^2 \rho r_x U}{k(U^2-a^2)} & \dfrac{UV-r_z a^2}{U^2-a^2} & 0 \\[3ex] \dfrac{\rho(r_z U-V)}{U^2-a^2} & \dfrac{r_y \rho U}{U^2-a^2} & \dfrac{r_x \rho U}{U^2-a^2} & \dfrac{k(V-r_z U)}{U(U^2-a^2)} & \dfrac{V}{U} \end{bmatrix} \quad (26a)$$

and $(A^{-1}C)$ by

$$A^{-1}C = \begin{bmatrix} \dfrac{UW-\phi_z a^2}{U^2-a^2} & \dfrac{-\phi_y a^2}{U^2-a^2} & \dfrac{-\phi_x a^2}{U^2-a^2} & \dfrac{k(\phi_z U-W)}{(U^2-a^2)} & 0 \\[3ex] 0 & \dfrac{W}{U} & 0 & \dfrac{\phi_y k}{\rho U} & 0 \\[3ex] 0 & 0 & \dfrac{W}{U} & \dfrac{\phi_x k}{\rho U} & 0 \\[3ex] \dfrac{a^2 \rho(\phi_z U-W)}{k(U^2-a^2)} & \dfrac{a^2 \rho \phi_y U}{k(U^2-a^2)} & \dfrac{a^2 \rho \phi_x U}{k(U^2-a^2)} & \dfrac{UW-a^2 \phi_z}{U^2-a^2} & 0 \\[3ex] \dfrac{\rho(\phi_z U-W)}{U^2-a^2} & \dfrac{\phi_y \rho U}{U^2-a^2} & \dfrac{\phi_x \rho U}{U^2-a^2} & \dfrac{k(W-\phi_z U)}{U(U^2-a^2)} & \dfrac{W}{U} \end{bmatrix} \quad (26b)$$

where a is the speed of sound and is equal to $\sqrt{\gamma p/(k\rho)}$ in terms of the nondimensional variables used in this report. The five eigenvalues of M are

$$\sigma^M_{1,2} = \frac{\partial \tau}{\partial \xi} \frac{\partial \xi}{\partial z} + \frac{UQ - m_z a^2 \pm a\sqrt{(U^2 - a^2)(m_y^2 + m_x^2) + (Q - m_z U)^2}}{U^2 - a^2} \tag{27a}$$

and

$$\sigma^M_{3,4,5} = \frac{\partial \tau}{\partial \xi} \frac{\partial \xi}{\partial z} + \frac{Q}{U} \tag{27b}$$

where

$$Q = \left(\frac{\partial \xi}{\partial r} V + \frac{\partial \xi}{\partial \phi} W \right) \frac{\partial \tau}{\partial \xi}$$

$$m_z = \left(\frac{\partial \xi}{\partial r} r_z + \frac{\partial \xi}{\partial \phi} \phi_z \right) \frac{\partial \tau}{\partial \xi}$$

$$m_y = \left(\frac{\partial \xi}{\partial r} r_y + \frac{\partial \xi}{\partial \phi} \phi_y \right) \frac{\partial \tau}{\partial \xi}$$

$$m_x = \left(\frac{\partial \xi}{\partial r} r_x + \frac{\partial \xi}{\partial \phi} \phi_x \right) \frac{\partial \tau}{\partial \xi}$$

The five eigenvalues of N are

$$\sigma^N_{1,2} = \frac{\partial \eta}{\partial \phi} \frac{UW - \phi_z a^2 \pm a\sqrt{(U^2 - a^2)(\phi_y^2 + \phi_x^2) + (W - \phi_z U)^2}}{U^2 - a^2} \tag{28a}$$

and

$$\sigma^N_{3,4,5} = \frac{\partial \eta}{\partial \phi} \cdot \frac{W}{U} \tag{28b}$$

Equations (27a) and (28a) are the slopes of the characteristics in the ζ,τ and ζ,η planes, respectively, while eqs. (27b) and (28b) are the slopes of the streamlines in their respective planes. The maximum modulus of eigenvalues used

27

in eq. (24) is then obtained from eqs. (27a) and (28a)

$$\sigma_M = |\sigma(M)|_{local \ max} = \max(|\sigma_1^M|, \ |\sigma_2^M|) \qquad (29a)$$

$$\sigma_N = |\sigma(N)|_{local \ max} = \max(|\sigma_1^N|, \ |\sigma_2^N|). \qquad (29b)$$

5. BOUNDARY AND INITIAL CONDITIONS

Several types of boundary conditions must be satisfied for the wing-body problem considered in this report. These include solid surfaces such as the wing-body surface, permeable surfaces such as the fitted outer bow shock wave, symmetry planes, and initial planes from which the computation can be started. Another type of boundary to consider is at points on the body where the transformation becomes singular; points such as the wing tip or wing-body juncture. In both of these locations the transformation metrics vanish or become infinite and the numerical procedure breaks down. The separate procedure devised to obtain the flow variables at these points is described below.

A. Body Surface

The success of the numerical scheme depends in a large part on the proper treatment of the surface boundary condition. For the inviscid flows considered in this report, the fluid velocity vectors on the body lie in the surface tangent planes. The scheme devised by Abbett, reference 7, is used to satisfy the surface tangency condition. The scheme which combines simplicity with accuracy is only applicable for steady supersonic flows. It treats the computation at the body in the same predictor-corrector fashion as the interior points and is, therefore, compatible with the rest of the calculations.

Abbett's scheme is a predictor-corrector procedure in which the values of the flow variables (u,v,w,p,ρ) are first

28

predicted at $\zeta^{n+1} = \zeta^n + \Delta\zeta$ using the MacCormack scheme and then these values are corrected using simple expansion or compression waves to enforce the surface tangency condition exactly. By restricting the flows to be steady and supersonic, Abbett is able to use the analytical solution of Prandtl-Meyer expansion.

The flow variables at $\zeta^{n+1} = \zeta^n + \Delta\zeta$ are predicted numerically by using eq. (17a) without the additional dissipation terms for the predictor step and eq. (19) for the corrector step. Decoding the conservative variables, call them $E_{3,k}^{(1)}$ from eq. (19) yields $u_{3,k}^{(1)}$, $v_{3,k}^{(1)}$, $w_{3,k}^{(1)}$, $p_{3,k}^{(1)}$, and $\rho_{3,k}^{(1)}$ at ζ^{n+1}.

The body surface is given by

$$f_b(z,r,\phi) = r - r_b(z,\phi) = 0$$
$$= r - 1 \qquad = 0 \tag{30}$$

The unit outward normal vector is in the left-handed Cartesian coordinate system

$$\vec{n}_b = \frac{\text{grad } f_b}{\left|\text{grad } f_b\right|} = \frac{-r_x\vec{i} - r_y\vec{j} - r_x\vec{k}}{(r_x^2 + r_y^2 + r_z^2)^{1/2}} \tag{31}$$

The surface tangency condition to be satisfied on the body is

$$\vec{q} \cdot \vec{n}_b = 0$$

or

$$ur_x + vr_y + wr_z = 0 \tag{32}$$

with the velocity vector given by its Cartesian components. The velocity vector at the surface

$$\vec{q}_{3,k}^{(1)} = u_{3,k}\vec{i} + v_{3,k}\vec{j} + w_{3,k}\vec{k} \tag{33}$$

predicted by the numerical scheme eqs. (17a) and (19) will not satisfy the tangency condition and will be rotated out of the

tangency plane by

$$\Delta\theta = \sin^{-1}\left[\vec{q}_{3,k}^{(1)} \cdot \vec{n}_b / q_{3,k}^{(1)}\right] \qquad (34)$$

where $q_{3,k}^{(1)}$ is the modulus of $\vec{q}_{3,k}^{(1)}$ and

$$\vec{q}_{3,k}^{(1)} \cdot \vec{n}_b = \frac{-u_{3,k}^{(1)}r_x - v_{3,k}^{(1)}r_y - w_{3,k}^{(1)}r_z}{\sqrt{r_x^2 + r_y^2 + r_z^2}} \qquad (35)$$

and the subscripts 3,k refer to the body surface. The flow can now be rotated according to the Prandtl-Meyer expansion or compression given the $\Delta\theta$. If $\Delta\theta$ is positive, an expansion is necessary to rotate $\vec{q}_{3,k}^{(1)}$ into the surface tangent plane and if $\Delta\theta$ is negative a compression is necessary.

If the rotation angle $\Delta\theta$ is small (under 5°), the following asymptotic expansion of the Prandtl-Meyer expansion, reference 10, gives the final corrected pressure at the surface

$$\rho_{3,k}^{n+1} = p_{3,k}^{(1)}\left[1 - \frac{\gamma(M_{3,k}^{(1)})^2}{\sqrt{(M_{3,k})^2-1}}\,\Delta\theta\right.$$

$$\left. + \gamma(M_{3,k}^{(1)})^2\left\{\frac{(\gamma+1)(M_{3,k}^{(1)})^4 - 4[(M_{3,k}^{(1)})^2-1]}{4[(M_{3,k}^{(1)})^2-1]^2}\right\}\Delta\theta^2\right] + 0(\Delta\theta^3) \quad (36)$$

where

$$M_{3,k}^{(1)} = \frac{q_{3,k}^{(1)}}{a_{3,k}^{(1)}} \quad \text{and} \quad a_{3,k}^{(1)} = \left[\frac{\gamma-1}{2}\,\frac{p_{3,k}^{(1)}}{\rho_{3,k}^{(1)}}\right]^{1/2}$$

Assuming the entropy to remain constant during the rotation of the velocity vector, the density $\rho_{3,k}^{n+1}$ can be determined from

$$\rho_{3,k}^{n+1} = (p_{3,k}^{n+1}/K)^{1/\gamma} \tag{37}$$

with $K = p_{3,k}^{(1)} / \left[\rho_{3,k}^{(1)}\right]^{\gamma}$.

The velocity magnitude is obtained from the energy equation, eq. (2),

$$q_{3,k}^{n+1} = (1 - p_{3,k}^{n+1}/\rho_{3,k}^{n+1})^{1/2}$$

It remains to find the individual Cartesian velocity components of $q_{3,k}^{n+1}$. Since the predicted velocity vector was rotated in the plane of itself and the surface normal vector, the direction of the final velocity vector is $\vec{n}_t$, that is,

$$\vec{q}_{3,k}^{n+1} \approx q_{3,k}^{n+1} \cdot \vec{n}_t$$

where

$$\vec{n}_t = \frac{\vec{q}_{3,k}^{(1)} - (\vec{q}_{3,k}^{(1)} \cdot \vec{n}_b)\vec{n}_b}{|\vec{q}_{3,k}^{(1)} - (\vec{q}_{3,k}^{(1)} \cdot \vec{n}_b)\vec{n}_b|} \tag{38}$$

The components are now easily obtained as

$$u_{3,k}^{n+1} = q_{3,k}^{n+1} \frac{\overline{M}}{[\overline{M}^2 + \overline{N}^2 + \overline{L}^2]^{1/2}}$$

$$v_{3,k}^{n+1} = q_{3,k}^{n+1} \frac{\overline{N}}{[\overline{M}^2 + \overline{N}^2 + \overline{L}^2]^{1/2}} \tag{39}$$

$$w_{3,k}^{n+1} = q_{3,k}^{n+1} \frac{\overline{L}}{[\overline{M}^2 + \overline{N}^2 + \overline{L}^2]^{1/2}}$$

where

$$\overline{M} = u_{3,k}^{(1)} - \frac{(u_{3,k}^{(1)} \cdot r_x + v_{3,k}^{(1)} \cdot r_y + w_{3,k}^{(1)} \cdot r_z) r_x}{| \quad |^2}$$

$$\overline{N} = v_{3,k}^{(1)} - \frac{(u_{3,k}^{(1)} \cdot r_x + v_{3,k}^{(1)} \cdot r_y + w_{3,k}^{(1)} \cdot r_z) r_y}{| \quad |^2}$$

$$\overline{L} = w_{3,k}^{(1)} - \frac{(u_{3,k}^{(1)} \cdot r_x + v_{3,k}^{(1)} \cdot r_y + w_{3,k}^{(1)} \cdot r_z) r_z}{| \quad |^2}$$

and

$$| \quad |^2 = r_x^2 + r_y^2 + r_z^2$$

This completes the boundary procedure for the body surface. It is essentially similar to the procedure described by Kutler, et al., reference 3. The most important difference, other than the different geometries considered and the generalized coordinate system, is the means by which the constant, K, eq. (37), is computed. In Kutler, et al.'s work K is assumed to be constant. For the configurations considered by them a single stagnation streamline wetted the entire body, hence the entropy on the body is fixed. However the assumption of constant entropy at the body is violated if crossflow shocks appear which intersect the body. They argue however that these cross-flow shocks are weak and will not significantly effect the solutions. Thus once the stagnation streamline is located, the body surface entropy and thus K is known immediately from the flow variables on any point on that streamline. Their work is restricted to nonseparated crossflows. In the present work the crossflow must separate, and, hence, the body is no longer wetted by a single stagnation streamline. The "constant", K, is no longer constant over the entire body since the entropy

is not constant. K must thus be determined numerically at
each point on the body surface.

B. Shock Surface

The boundary condition at the shock surface is similarly
treated as at the body surface except that the Rankine-Hugoniot
conditions must be satisfied instead of the flow tangency con-
dition. Specifically we need to determine the shock surface.
Let the shock surface be given by

$$f_s(z,r,\phi) = r - r_s(z,\phi) = 0 \tag{40}$$

The outward unit normal is given in terms of the left-handed
Cartesian unit vectors by (see fig. 6)

$$\vec{n}_x = \frac{-1}{|\nabla f_s|} \left\{ (r_x - r_{s\phi}\phi_x)\vec{i} + (r_y - r_{s\phi}\phi_y)\vec{j} + (r_z - r_{sz} - r_{s\phi}\phi_z)\vec{k} \right\} \tag{41}$$

where

$$|\nabla f_s| = [(r_x - r_{s\phi}\phi_x)^2 + r_y - r_{s\phi}\phi_y)^2 + (r_z - r_{sz} - r_{s\phi}\phi_z)^2]^{1/2}$$

The metrics $r_x, r_y, r_z, \phi_x, \phi_y,$ and ϕ_z are known once r and ϕ of
the shock surface are known. The preshock velocity vectors
normal and tangential to the shock surface are

$$\vec{u}_1 = -(\vec{q}_\infty \cdot \vec{u}_s)\vec{n}_s \tag{42}$$

and

$$\vec{\tilde{v}}_1 = \vec{q}_\infty - \vec{u}_1, \text{ respectively} \tag{43}$$

The notation used in this section is as follows: Subscript 1
or ∞ denotes preshock condition, subscript 2 - postshock,
superscript tildas on u and v denote the velocity vectors

33

normal and tangential to the shock surface, respectively. The
magnitude of the normal preshock velocity vector is

$$
\tilde{u}_1 = (q_\infty \cdot \vec{n}_s) \sqrt{\vec{n}_s \cdot \vec{n}_s}
$$

$$
= \frac{1}{|\nabla f_s|^2} \left\{ (r_x - r_{s\phi}\phi_x)u_\infty + (r_y - r_{s\phi}\phi_y)v_\infty \right.
$$

$$
\left. + (r_z - r_{sz} - r_{s\phi}\phi_z)w_\infty \right\} |\nabla f_s| \qquad (44)
$$

Squaring and cancelling obtains

$$
\tilde{u}_1^2 |\nabla f_s|^2 = \left\{ (r_x - r_{s\phi}\phi_x)u_\infty + (r_y - r_{s\phi}\phi_y)v_\infty + (r_z - r_{sz} - r_{s\phi}\phi_z)w_\infty \right\}^2
$$

Solve now for r_{sz} to obtain

$$
r_{sz} = (r_z - r_{s\phi}\phi_z) + w_\infty\Omega + \tilde{u}_1 \sqrt{\Omega^2 + \{ \ \}/(w_\infty^2 - \tilde{u}_1^2)} \qquad (45)
$$

where

$$
\Omega = \frac{(r_x - r_{s\phi}\phi_x)u_\infty + (r_y - r_{s\phi}\phi_y)v_\infty}{w_\infty^2 - \tilde{u}_1^2}
$$

$$
\{ \ \} = (r_x - r_{s\phi}\phi_x)^2 + (r_y - r_{s\phi}\phi_y)^2
$$

The shock wave is moved according to the following Euler
predictor and modified Euler corrector:

<u>Predictor</u>: $\qquad r_s^{\overline{n+1}} = r_s^n + r_{sz}^n \, \Delta\zeta^{n+1}$ $\qquad\qquad\qquad$ (46)

<u>Corrector</u>: $\qquad r_s^{n+1} = r_s^n + \frac{1}{2}\left[r_{sz}^n + r_{sz}^{(\overline{n+1})} \right]\Delta\zeta^{n+1}$ $\qquad\qquad$ (47)

34

where $\Delta\zeta$ is the integration stepsize. The quantities $r_{s\phi}$ are evaluated by simple one-sided differencing

$$r_{s\phi}^{\overline{n+1}} = \left(r_{s_{NT2,KPL}}^{\overline{n+1}} - r_{s_{NT2,KPR}}^{\overline{n+1}} \right) \Big/ \left(\phi_{NT2,KPL} - \phi_{NT2,KPR} \right) \quad (48)$$

and

$$r_{s\phi}^{n+1} = \left(r_{s_{NT2,KCL}}^{n+1} - r_{s_{NT2,KCR}}^{n+1} \right) \Big/ \left(\phi_{NT2,KCL} - \phi_{NT2,KCR} \right) \quad (49)$$

The subscript indices have been previously defined. The procedure for determining the shock slope is as follows: the postshock conditions are predicted using eq. (20a) and eq. (46). Decoding obtains a predicted postshock pressure, p_2, from which the normal preshock velocity is given for a perfect gas by

$$\tilde{u}_1^2 (p_2; \; p_\infty, \rho_\infty) = \frac{p_\infty}{2\rho_\infty} \left[\frac{\gamma^2 - 1}{2\gamma} \frac{p_2}{p_\infty} + (\gamma - 1) \right] \quad (50)$$

Forming the metrics from the predicted $r_s^{\overline{n+1}}$ and $r_{s\phi}^{\overline{n+1}}$ from eq. (48) gives sufficient information to solve for the shock slope using eq. (45). The postshock velocity vector can now be determined from

$$\vec{q}_2 = \vec{\tilde{u}}_2 + \vec{\tilde{v}}_2 \quad (51)$$

where $\vec{\tilde{u}}_2$ and $\vec{\tilde{v}}_2$ are the postshock normal and tangential velocity components. The tangential component remains unchanged across the shock, thus

$$\vec{\tilde{v}}_2 = \vec{\tilde{v}}_1 \quad (52)$$

and the normal component is determined by use of the continuity equation

$$\tilde{u}_2 = \tilde{u}_1 \rho_1 / \rho_2 \quad (53)$$

and ρ_2 is given by the Rankine-Hugoniot condition

$$\rho_2(p_2;\ p_\infty,\rho_\infty)\ =\ \rho_\infty\ \frac{\dfrac{p_2}{p_\infty}\ +\ \dfrac{\gamma-1}{\gamma+1}}{1\ +\ \dfrac{\gamma-1}{\gamma+1}\dfrac{p_2}{p_\infty}} \tag{54}$$

The normal postshock velocity is given by

$$\vec{q}_2\ =\ u_2\vec{i}\ +\ v_2\vec{j}\ +\ w_2\vec{k}$$

$$=\ \vec{q}_\infty\ -\ \left(1\ -\ \frac{\rho_1}{\rho_2}\right)\ \tilde{u}_1\vec{n}_s \tag{55}$$

which can be broken into the requisite Cartesian postshock velocity components u_2, v_2, w_2. This completes the predictor step. The entire procedure is repeated for the corrector step except that the appropriate equations to be used are now (20b), (47), and (49).

C. Symmetry Plane

The flow fields of interest in this report have a plane of bilateral symmetry since no yaw angles are considered and the configurations considered are bilaterally symmetric. This allowed us to reduce the number of mesh points required. The symmetry conditions are imposed by simple reflection of the flow variables and the outer bow shock location about the two planes of symmetry $\phi = 0°$ and $\phi = 180°$. Since MacCormack's scheme is a noncentered predictor-corrector scheme, it is not possible to apply the symmetry conditions after the predictor step. The predicted values of the flow variables are obtained directly by applying the predictor step eq. (17a), to the point beyond the symmetry planes, i.e. $\phi = 0° - \Delta\phi$ and $\phi = 180° + \Delta\phi$.

36

The symmetry conditions are imposed only after the corrector step to provide sufficient information for the predictor step for the next marching step.

Treating the symmetry planes in this manner avoids the spurious oscillations emanating from the symmetry planes. These oscillations occur when MacCormack's scheme is employed with a generalized curvilinear coordinate system and symmetry is imposed after both the predictor and corrector steps.

D. Wing-Tip Condition

At the wing-tip the transformed Euler equations, eq. (6) are indeterminate. This can be shown as follows: the basic equations are eqs. (4) along with the contravariant velocity components, eqs. (5). The appropriate metrics are given by eqs. (6). If we now consider the region near the wing tip

$$r = 1 + \epsilon \qquad |\epsilon| << 1$$

and

$$\theta \sim \theta \qquad |\theta| << 1 \tag{56}$$

where $\phi - \pi/2 = \theta$, we can write the metrics in asymptotic form as

$$x_r = \tilde{a}\epsilon \qquad x_\theta = -\tilde{a}\theta$$
$$y_r = \tilde{a}\epsilon \qquad y_\theta = \tilde{a}\epsilon \tag{57}$$

where

$$\tilde{a} = \frac{R}{2} \left\{ 1 \pm \frac{1}{\sqrt{1 - 4B^2/R^2}} \right\} \tag{58}$$

and the Jacobian is

$$J^{-1} = \tilde{a}^2(\epsilon^2 + \theta^2) \tag{59}$$

37

With these metrics, the asymptotic form of the governing
equations becomes

$$\rho_\epsilon \overline{V} + \rho_\theta \overline{W} + \rho C + \rho D = 0$$

$$(\rho u)_\epsilon \overline{V} + (\rho u)_\theta \overline{W} + \rho u (C+D) = 0$$

$$(\rho v)_\epsilon \overline{V} + (\rho v)_\theta \overline{W} + \rho v (C+D) = 0$$

$$(\rho w)_\epsilon \overline{V} + (\rho w)_\theta \overline{W} + \rho w (C+D) + \epsilon_z k p_\epsilon + \theta_z k p_\theta = 0$$

where the overbar $(\overline{})$ stands for $J^{-1}(\ )$

$$C = \tilde{a} [\epsilon u_\epsilon + \theta v_\epsilon + w_\epsilon (-\theta y_z + \epsilon x_z)]$$

and

$$D = \tilde{a} [-\theta u_\theta + \epsilon v_\theta + w_\theta (x_z \theta - y_z \epsilon)]$$

All of the overbarred quantities vanish as $\epsilon, \theta \rightarrow 0$. Thus as
the wing tip is approached, the basic equations are always
satisfied provided the flow variables are continuous. Thus
the Euler equations can be satisfied by any continuous values
of the primitive variables at the wing tip.

If we now allow for discontinuous solutions of the Euler
equations at the wing tip we have

$$[\tilde{E}] \cos(n,z) + [\tilde{F}] \cos(n,r) + [\tilde{G}] \cos(n,\phi) = 0$$

where the $\cos(n,z)$, $\cos(n,r)$, and $\cos(n,\phi)$ are direction
cosines between the coordinates and the surface of discontin-
uity. From the previous asymptotic forms of the metrics, the
jump relations to the lowest order become

38

$$[\rho\overline{V}] \cos(n,r) + [\rho\overline{W}] \cos(n,\phi) = 0$$

$$[\rho u\overline{V} + y_\theta kp] \cos(n,r) + [\rho u\overline{W} - y_r kp] \cos(n,\phi) = 0$$

$$[\rho v\overline{V} - x_\theta kp] \cos(n,r) + [\rho v\overline{W} + x_r kp] \cos(n,\phi) = 0$$

$$[\rho w\overline{W} + \varepsilon_z kp] \cos(n,r) + [\rho w\overline{W} + \theta_z kp] \cos(n,\phi) = 0$$

Since all the metrics and the overbarred quantities vanish at the tip, it follows that the jump relations are identically satisfied there.

Thus for both discontinuous and continuous flows, the Euler equations are indeterminate at the wing tip. In other words arbitrary values can be set for ρ, u, v, w at the wing tip.

Since we are free to pick the primitive flow variables at the wing tip, we can be guided by the actual physics of the flow. We will model the flow of a vortex sheet coming off tangentially to the wing at the tip. It is well known that for compressible flows that tangency cannot be satisfied for positive pressures and densities if the flow must turn 180° as at the wing tip. Thus we require the flow to separate. Even though the equations are indeterminate at the wing tip, the primitive variables must satisfy the jump relations for the untransformed Euler equations and these are for a tangential vortex sheet

    (i) p is continuous
   (ii) $v = 0$ (i.e. the sheet is a streamline)
  (iii) total enthalpy is constant

The jump in the tangential velocity $\left[\sqrt{u^2 + w^2}\right]$ across the sheet is arbitrary. The jump in density is then determined from the constancy of total enthalpy.

39

Two more conditions are required before all the flow
variables are determined at the wing tip.

The two additional conditions that we have used with
partial success are:

(iv) $u/w = \tan(\psi - \psi_o)$

(v) $p/\rho^\gamma = $ constant

where ψ is the leading-edge sweep angle. In particular we set
$\psi_o \equiv \psi_m$, i.e. the flow at the tip follows the mean flow direc-
tion obtained by averaging the flow directions just inboard of
the tip on the upper and lower surfaces. These five conditions
are similar to those utilized by Minailos (ref. 12) except that
he set ψ_o so as to obtain good agreement with experimental data.

These conditions are implemented into the code as follows:

a) $p_o = 0.5(p_1 + p_{-1})$ b) $\rho_o = 0.5(\rho_1 + \rho_{-1})$

c) $v_o = 0$ d) $\psi_o = 0.5(\psi_1 + \psi_{-1})$

e)   total enthalpy is constant

where subscript "o" designates the wing tip, "1" the first point
on the upper surface inboard of the tip and "-1" the first point
on the lower surface inboard of the wing tip. In other words
the pressure, density, and flow angle at the wing tip are
obtained by averaging over the nearest surface neighboring
values. The reason for averaging the density instead of using
condition (v) is that the latter condition requires an accurate
evaluation of the surface entropy. This was not possible with
the present code. An alternate boundary condition for deter-
mining the densities on each side of the vortex sheet would be
to specify the rate of vortex shedding from the leading edge.
From this information the velocity on each side of the sheet
would be given and the densities could then be calculated.
This is unlike two-dimensional airfoil theory where conditions

40

(i), (ii) and (iii) fix the strength of the vortex sheet. The reason for this is that in two-dimensional flows the wake consists of a single split streamline whereas for three-dimensions the vortex sheet consists of separate streamlines from the top and bottom surfaces which may be of different entropies.

E. Wing-Body Juncture

At the wing-body juncture, the transformation metrics (eq. (16)) become singular since the term under the radical sign vanishes.

This singular behavior is due to the abrupt jump of the surface slope between the body and the wing. As mentioned in section 3, this singular behavior can be automatically avoided if the analytical expressions, eq. (16), for the metrics are replaced by their finite difference equivalent. No special treatment will then be required at these points as was required for the singularity at the wing-tip.

However to replace the analytic expressions by their finite difference expression is impractical in context of the existing Space Shuttle code, refs. 3 and 4. In that code the transformation of the physical body to a unit radius cylinder as given by eq. (16) and the normalization of the distance between the body surface and shock surface as given by eq. (7) are treated as two separate transformations. The mesh point coordinates from which the finite differences would be computed are determined only as the net result of both transformations. Thus there is no straightforward procedure for computing the metrics, eq. (16), numerically.

The procedure used in this report is to avoid the wing-body juncture singularity. This is done by filleting the juncture to eliminate the abrupt change in surface slope. The simplest method of achieving this is to add a small perturbation

41

to the transformed body radius, so that instead of $r_b(z,\phi) = 1$, we have $r_b(z,\phi) = 1 + \varepsilon$. The perturbation, ε, used herein is 0.025. With this perturbation the wing-body configuration shown in figure 5a is obtained.

F. Initial Starting Plane Conditions

The starting solution or initial data plane can be obtained by one of two ways. The Space Shuttle code has the capability to generate internally the solution for a pointed cone at angle of attack using the shock-fitting procedure. To start that solution all the grid points in the initial plane are initialized using the analytical solution for a pointed cone at zero degree angle-of-attack and the given free-stream Mach number. The integration is started and the angle of attack is incremented over 100 marching steps to its final value. Thereafter the integration is continued until the calculation has converged to a conical flow field solution. Since the flow is conical, the axial coordinate is stepped back to its original starting value to give the starting plane flow field for a pointed cone at angle-of-attack. This procedure was used to provide the initial data for the wing-body configurations studied in this report.

For the delta wing alone, a slightly different procedure is required. Starting with a given wing-body solution of the desired sweep angle, angle-of-attack, and free-stream Mach number, the integration procedure is continued while the physical body radius is gradually forced to vanish over twenty to thirty marching steps. Thereafter the transformed body radius, $r_b(z,\phi)$, is forced slowly to unity over another twenty steps. The integration continues until again a conical flow field is obtained. If solutions are required for planar wings other than delta wings, then the conical planar delta wing solution is used as a starting solution and the sweep angle can vary arbitrarily with the axial coordinate, z.

42

6. NUMERICAL RESULTS AND DISCUSSION

Numerical calculations have been obtained for two cases: a planar delta wing alone of aspect ratio 1.0 at free-stream Mach number 3 and angle of attack $\alpha = 10°$, and a delta wing in the presence of a circular body at $M_\infty = 3$ and $\alpha = 10°$.

A. Wing Alone

The first numerical results are for delta wing alone at $M_\infty = 3$ and $\alpha = 10°$. The closest available experimental data, reference 13, are for a configuration shown in figure 7(a). This experimental configuration has a finite thickness delta wing with the edges beveled to obtain sharp leading and trailing edges. The experimental free-stream Mach number is 2.86. The pressure coefficients are shown in figure 7(b). The effects of thickness have been subtracted out of the experimental results shown. The present Euler code results and the experimental data compare quite well except near the tip. The effects of the bevel at the tip of the experimental configuration cause some scatter in the data. The cause of the spikes in the numerical pressure coefficients is not clear. It is suspected that they are a result of the nonlinear instability of MacCormack's scheme at the tangential discontinuity at the wing tip. The lift coefficients are 0.222 and 0.215 for the Euler code and experimental results, respectively.

The conical streamline plot, figure 8, shows the location of the two vortical singularities and the stagnation stream surface. Vortical singularities occur at the windward plane of symmetry and above the upper surface 30% of the span inboard of the leading edge. The stagnation stream surface is on the lower surface about 1% span inboard of the wing tip. These results show that the Kutta condition imposed at the wing leading edge cause the flow to separate from the tip tangentially to the surface. There are no experimental data such as vapor

43

screen data for this angle of attack and Mach number to verify
the location of the leading-edge vortex for a thin delta wing.
Figure 9 shows the particle paths obtained by the numerical
results as would be seen by a vapor-screen visualization. The
flow field for the delta wing are shown in figure 10. Shown
are the Cartesian crossflow velocity vectors.

B.   Wing-Body

The results for the wing-body calculation are shown in
figures 11(a) to (c), in terms of pressure coefficients at
stations just before the wing, at the wing trailing edge, and
midway between these two. Figure 11(a) shows the rapid
expansion around the windward side of the cylinder terminating
with a strong crossflow shock wave followed by some isentropic
compression on the leeside. Figure 11(b) shows that the cross-
flow initially expands around the body but then must recompress
to meet the wing-body juncture. The flow continues to compress
as the crossflow stagnation point is reached on the windward
side of the wing just inboard of the leading edge. Rapid
expansion around the leading edge follows and then gradual
recompression on the leeside of the wing and body. Figure 11(c)
showing the pressure distribution at the trailing edge of the
wing shows a continuation of these events. The lift coefficient
based on the wing planform area of the wing panel alone in the
presence of the body is 0.237.

The large oscillations of the pressure coefficient seen
near the juncture of the wing and body seem disturbing at first.
However their origin can be pinpointed to the poor mesh resolu-
tion at the juncture. This is a basic fault of any type of
conformal transformations such as those used in this report.
Coordinate lines are quite strongly concentrated at convex
corners such as the wing tip and quite dispersed at concave
corners. This can be readily observed in figure 5. This
problem can be easily solved by obtaining the mesh points by

44

some other means than the conformal transformation. However
this will require writing essentially a new computer code so
that the transformation metrics may be computed numerically.
As mentioned previously this is incompatible with the present
code.

The particle paths as would be seen by vapor screen visu-
alization is shown in figure 12. Again the flow is seen to be
leaving the leading edge tangentially to the lower surface.

C. Wing-Body Interference

The final figure shows the wing-body interference factor,
K_w, obtained experimentally (ref. 1) and by the present results.
This factor is the ratio of the lift on the wing panels mounted
on the body to the lift of the wing alone for the same angles
of attack. Slender-body theory indicates that a favorable
interference factor of $K_w = 1.45$ is obtained on the wing lift
by the presence of the body. Compressibility effects reduce
this favorable interference to 1.07 obtained by the present
Euler code and Kutta condition compared to 0.98 experimentally.
Although the airfoil section differ for the numerical and
experimental results, the adverse effect of compressibility
on wing-body interference is predicted fairly well.

7. CONCLUSIONS AND RECOMMENDATIONS

The specific results obtained in this study are as
follows:

a) The lifting coefficients and flow field data of a
$M_\infty = 3$ planar delta wing at an angle-of-attack
$\alpha = 10°$ have been obtained. The normal-force coef-
ficient compares well with the experimental
coefficient (at $M_\infty = 2.86$ and finite thickness wing)
of 0.215.

b)   The normal-force coefficient, flow field data, and the
     interference coefficient have been obtained for a
     delta wing in the presence of a circular body at
     $M_\infty = 3.0$ and $\alpha = 10°$. The normal-force coefficient
     based on the wing panel planform area is 0.237. The
     interference coefficient $K_w = 1.07$ as compared to the
     experimental $K_w = 0.98$ for a wing-body configuration
     with slightly different airfoil sections for the wing
     panel.

A number of conclusions may be drawn from this study.
Good flow field and surface pressure results are obtainable
for wings alone and wing-body configurations with sharp leading
edges by combining an Euler equation solver with a Kutta con-
dition to simulate the viscous effects at the leading edges.
The separation and leading-edge vortex seem to be properly
predicted. However no flow field comparisons with experimental
data were made due to the lack of experimental flow field data.
Presently the speed of the code is controlled by the fine mesh
at the tip and the accuracy by the coarse mesh at the juncture.
Thus the numerical procedure can be considerably speeded up and
the accuracy substantially improved by a better distribution of
mesh points. The additional dissipation appended to MacCormack's
scheme to control the severe nonlinear instability near the wing
leading edge is sufficient to stabilize the scheme. But it is
not known whether it may be too dissipative and diffuse the
vorticity too rapidly. It should be noted that the application
of the Kutta condition is also possible for flows with subsonic
axial Mach numbers.

Two recommendations seem appropriate. The code should be
revised so that the metrics are obtained numerically to allow
for a more arbitrary clustering of mesh points where necessary,
i.e., more at the wing-body juncture and fewer at the wing tip.
The conformal transformation presently used clusters too much

46

at the tip and disperses too much at the juncture. Also a more careful and thorough study is required to determine the best stabilizing terms to be added to MacCormack's scheme. This dissipation should be localized to the region where needed.

REFERENCES

1. Nielsen, J.N.: Nonlinearities in Missile Aerodynamics.
   AIAA Paper No. 78-20, Invited paper, AIAA 16th Aerospace
   Sciences Meeting, Huntsville, AL, Jan. 16-18, 1978
   (also NEAR Paper No. 63).

2. Nielsen, J.N.: <u>Missile Aerodynamics</u>. McGraw-Hill Book
   Co., Inc., New York, 1960, p. 119.

3. Kutler, P., Warming, R.F. and Lomax, H.: Computation of
   Space Shuttle Flowfields Using Noncentered Finite-
   Difference Schemes. AIAA Journal, Vol. 11, No. 2,
   Feb. 1973, pp. 196-204.

4. Kutler, P. and Lomax, H.: Shock-Capturing, Finite Dif-
   ference Approach to Supersonic Flows. J. of Spacecraft
   & Rockets, Vol. 8, No. 12, Dec. 1972, pp. 1175-1187.

5. Parker, A.G.: Aerodynamic Characteristics of Slender
   Wings with Sharp Leading Edges - A Review. J. of Aircraft,
   Vol. 13, No. 3, March 1976.

6. Vigneron, V.C., Rakich, J.V., and Tannehill, J.C.: Calcula-
   tion of Supersonic Viscous Flow Over Delta Wings with Sharp
   Subsonic Leading Edges. AIAA Paper No. 78-1137, AIAA 16th
   Aerospace Sciences Meeting, Huntsville, AL, Jan. 16-18,
   1978.

7. Abbett, M.J.: Boundary Condition Computational Procedures
   for Inviscid Supersonic Steady Flow Field Calculations.
   Aerotherm Corp., Mountain View, CA, Final Report, 71-41,
   1971.

8. Viviand, H.: Conservative Forms of Gas Dynamic Equations.
   La Recherche Aerospatiale, No. 1, Jan.-Feb. 1974, pp. 65-
   68.

9. Kutler, P.: Application of Selected Finite Difference
    Techniques to the Solution of Conical Flow Problems.
    Ph.D. Thesis, Dept. of Aerospace Engineering, Iowa State
    University, Ames, Iowa, 1969.

10. Ames Research Staff: Equations, Tables, and Charts for
    Compressible Flow. NACA Rept. 1135, 1953.

11. Baldwin, B.S. and MacCormack, R.W.: Interaction of Strong
    Shock Wave with Turbulent Boundary Layer. Proceedings
    of the Fourth International Conference on Numerical
    Methods in Fluid Dynamics, Springer-Verlag Lecture Notes
    in Physics, No. 35, June 1974.

12. Minailos, A.N.: Calculation of Supersonic Flow Past Wings
    with Consideration of Tangential Discontinuities Shed
    from the Edges within the Scope of a Model Using a System
    of Euler Equations. Fluid Dynamics, Vol. 13, No. 1,
    Jan.-Feb. 1978.

13. Stallings, R.: NASA/Langley Research Center, unpublished
    data on delta wings at supersonic flows, 1979.

APPENDIX A

CARTESIAN AND CONICAL PARTICLE PATHS

A detailed discussion is given in this appendix on the
method of obtaining the Cartesian and conical particle paths
projected on a constant z-plane.

Cartesian Streamline/Particle Path Plots

The Cartesian crossflow velocity vectors projected on the
constant z-plane trace out "pseudo" streamlines. These stream-
lines represent steady state path lines of fluid particles.
The path lines are determined by solving the differential
equation

$$\frac{dx}{dt} = u(x,y) \tag{A-1}$$

$$\frac{dy}{dt} = v(x,y) \tag{A-2}$$

A modified Euler-Cauchy method is used to solve these
equations in the form

$$\Delta x = x^* - x_{j,k} = \int_{t}^{t+\Delta t} u(x,y)dt \tag{A-3}$$

$$\Delta y = y^* - y_{j,k} = \int_{t}^{t+\Delta t} v(x,y)dt \tag{A-4}$$

where x^* and y^* are the projected locations of the next point
on the streamline curve. The integration is started after an
incremental time step, Δt, has been defined and the initial
position of the fluid particles at arbitrarily selected point
have been established.

51

The numerical integration is started by initially assuming that u and v at (j,k) are constant over the interval $x_{j,k} \leq x \leq x_{j+1,k+1}$ and $y_{j,k} \leq y \leq y_{j+1,k+1}$. This results in a preliminary estimate of x* and y* of

$$x^* = x_{j,k} + u\Delta t \qquad (A-5)$$

$$y^* = y_{j,k} + v\Delta t \qquad (A-6)$$

The velocity components at (j*,k*) are determined by linear interpolation as illustrated in the sketch below. We need to
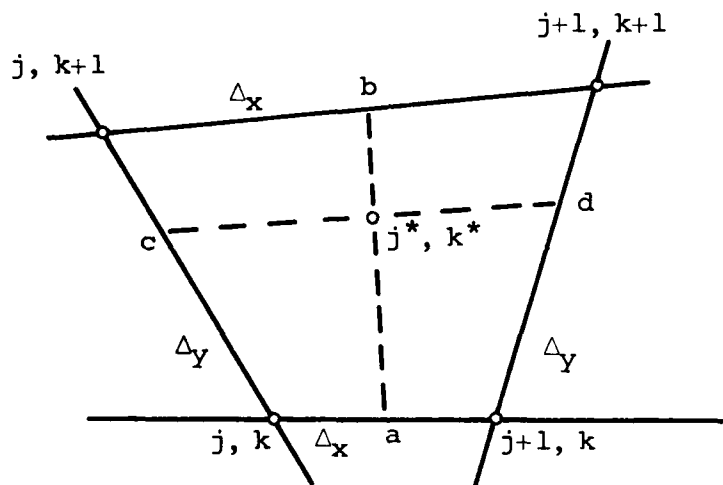
determine Δ_x and Δ_y which are defined by any of eqs. (A-9) and (A-10), respectively. We have

$$\frac{x^* - x_a}{x_b - x_a} = \frac{y^* - y_a}{y_b - y_a} \qquad (A-7)$$

and

$$\frac{x^* - x_c}{x_d - x_c} = \frac{y^* - y_c}{y_d - y_c} \qquad (A-8)$$

where

$$x_a = (1 - \Delta_x)x_{j,k} + \Delta_x\, x_{j+1,k}$$

$$y_a = (1 - \Delta_x)y_{j,k} + \Delta_x\, y_{j+1,k}$$

$$x_b = (1 - \Delta_x)x_{j,k+1} + \Delta_x\, x_{j+1,k+1} \qquad\qquad \text{(A-9)}$$

$$y_b = (1 - \Delta_x)y_{j,k+1} + \Delta_x\, y_{j+1,k+1}$$

$$x_c = (1 - \Delta_y)x_{j,k} + \Delta_y\, x_{j,k+1}$$

$$y_c = (1 - \Delta_y)y_{j,k} + \Delta_y\, y_{j,k+1}$$

$$x_d = (1 - \Delta_y)x_{j+1,k} + \Delta_y\, x_{j+1,k+1} \qquad\qquad \text{(A-10)}$$

$$y_d = (1 - \Delta_y)y_{j+1,k} + \Delta_y\, y_{j+1,k+1}$$

Solving eqs. (A-7) and (A-9) for Δ_x obtains

$$\Delta_x = \frac{-\beta_x + \sqrt{\beta_x^2 - 4\alpha_x\gamma_x}}{2\alpha_x} \qquad\qquad \text{(A-11)}$$

where

$$\alpha_x = (x_{j+1,k} - x_{j,k})(y_{j,k+1} - y_{j+1,k+1})$$

$$\quad - (x_{j,k+1} - x_{j+1,k+1})(y_{j+1,k} - y_{j,k})$$

$$\beta_x = - (x_{j+1,k} - x_{j,k})(y_{j,k+1} - y_{j,k})$$

$$\quad - (x_{j*,k*} - x_{j,k})(y_{j+1,k} - y_{j,k} + y_{j+1,k} - y_{j+1,k+1})$$

$$\quad + (y_{j+1,k} - y_{j,k})(x_{j,k+1} - x_{j,k}) \qquad\qquad \text{(A-12)}$$

$$\quad - (y_{j*,k*} - y_{j,k})(x_{j+1,k} - x_{j,k} - x_{j+1,k+1} + x_{j,k+1})$$

$$\gamma_x = (x_{j*,k*} - x_{j,k})(y_{j,k+1} - y_{j,k})$$

$$\quad - (y_{j*,k*} - y_{j,k})(x_{j,k+1} - x_{j,k})$$

53

Similarly eqs. (A-8) and (A-10) are solved for Δ_y to obtain

$$\Delta_y = \frac{-\beta_y + \sqrt{\beta_y^2 - 4\alpha_y \gamma_y}}{2\alpha_y} \tag{A-13}$$

where α_y, β_y, and γ_y are the same as α_x, β_x, γ_x with the points (j,k+1) and (j+1,k) interchanged.

The interpolated velocity components are now easily obtained as

$$u_{j*,k*} = (1 - \Delta_x)(1 - \Delta_y)u_{j,k} + \Delta_x(1 - \Delta_y)u_{j+1,k}$$
$$+ \Delta_x\Delta_y\, u_{j+1,k+1} + (1 - \Delta_x)\Delta_y\, u_{j,k+1} \tag{A-14}$$

and

$$v_{j*,k*} = (1 - \Delta_x)(1 - \Delta_y)v_{j,k} + \Delta_x(1 - \Delta_y)v_{j+1,k}$$
$$+ \Delta_x\Delta_y\, v_{j+1,k+1} + (1 - \Delta_x)\Delta_y\, v_{j,k+1} \tag{A-15}$$

By averaging the appropriate velocity components at (j*,k*) with those at (j,k), an improved estimate of x* and y* is obtained. This improved estimate is

$$x* = x_{j,k} + \frac{1}{2}(u_{j,k} + u_{j*,k*})\Delta t \tag{A-16}$$

$$y* = y_{j,k} + \frac{1}{2}(v_{j,k} + v_{j*,k*})\Delta t \tag{A-17}$$

The velocities at the new (j*,k*) are recomputed, as above, and then the new location and velocity vector are used as the initial conditions for calculating the next point. The process is repeated until the maximum number of time steps is reached.

54

Conical Streamline/Particle Path Plot

For conical bodies such as delta wings it is more conven-
ient to use conical streamlines than the Cartesian crossflow
streamlines as developed above. It is a simple matter to
modify the above procedure to obtain the conical streamline
plot. The procedure detailed below will not give a strictly
correct streamline crossflow but the error is negligible.

Suppose the vertex of the conical body is at Z_o and that
the crossflow data are available at Z_p as shown in the sketch
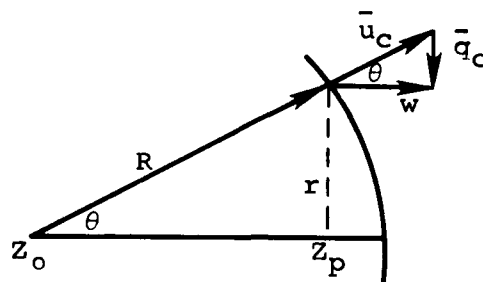below.
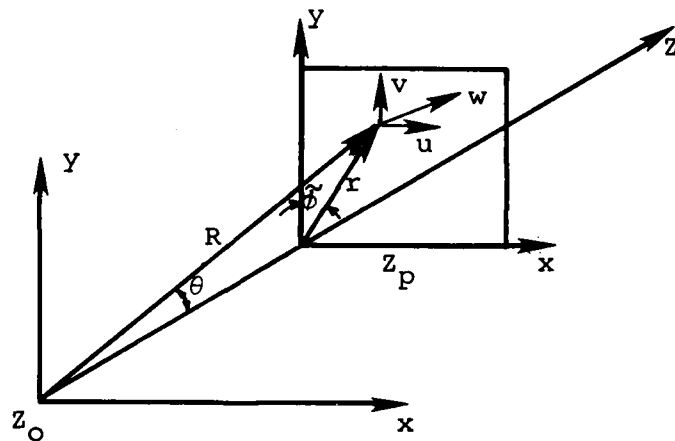
At each point (x,y) in the Z_p-plane the three Cartesian
velocity components are given. We do not have the data given
on a constant R surface as required for a true conical projec-
tion. However the errors will be small for $Z_p - Z_o \gg r$. The
required relations for r, θ, and $\tilde{\phi}$ are given by

$$r = \sqrt{x^2 + y^2}$$

$$\theta = \tan^{-1}[r/(Z_p - Z_o)] \qquad \text{(A-18)}$$

$$\tilde{\phi} = \tan^{-1}[x/y]$$

We require the (x,y) components of the conical crossflow velocity components so that the procedure of the previous section can be employed. These components are derived by resolving the w component into a component, call it $\bar{u}_c$, along the conical ray R and a component, $\bar{q}_c$, in the Z_p-plane as shown in the sketch below.

These components are given by

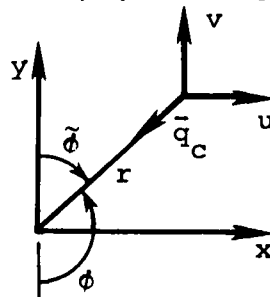$$\bar{u}_c = w/\cos \theta \qquad\qquad (A-19)$$

and

$$\bar{q}_c = w \tan \theta \qquad\qquad (A-20)$$

The (x,y) components of $\bar{q}_c$ are given by (see sketch below)

$$\bar{q}_{cx} = - \bar{q}_c \sin \tilde{\phi}$$

and

$$\bar{q}_{cy} = - \bar{q}_c \cos \tilde{\phi}$$

Adding these components to the Cartesian crossflow velocity components obtains the Cartesian components of the conical crossflow velocity vector projected on the constant Z_p-plane, i.e.,

$$u_c = u - \bar{q}_c \sin \tilde{\phi} \qquad\qquad \text{(A-21)}$$

$$v_c = v - \bar{q}_c \cos \tilde{\phi}$$

These velocity components are to be used in place of u,v of
the previous section to obtain the conical streamline path,
an example of which is shown in figure 8.

LIST OF SYMBOLS

$\cancel{R}$	aspect ratio
$A^{-1}B$	matrix defined by eq. (26a)
$A^{-1}C$	matrix defined by eq. (26b)
a	speed of sound, $\sqrt{\gamma p / k \rho}$
$\tilde{a}$	parameter defined by eq. (58)
B	body radius in Cartesian space
C,D	parameters defined following eq. (59)
C_m, C_v	damping coefficients, defined following eq. (18)
CFL	Courant-Friedricks-Lewy number
$\hat{E}, \hat{F}, \hat{G}$	column vectors in Cartesian space (eq. (1))
$\tilde{E}, \tilde{F}, \tilde{G}$	column vectors in transformed space (eq. (4))
(E,F,G,H)	column vectors in computational space (eq. (9))
e_i	components of E
f	clustering function in meridional direction (eq. (7))
f_b	function describing the transformed body surface
f_s	function describing the transformed shock surface
g	$= x + iy$
h	clustering function in radial direction (eq. (7))
i	$= \sqrt{-1}$
$\vec{i}, \vec{j}, \vec{k}$	Cartesian unit vectors
I	identity matrix
J	Jacobian
j,k	indices in the computational mesh system (fig. 5)
K	constant defined by eq. (37)

K_w	interference factor
KCL,KCR	index parameters, defined by eq. (17)
KPL,KPR	index parameters, defined by eq. (17)
k	$= 2\gamma/(\gamma-1)$; or index in computational space
$\overline{L},\overline{M},\overline{N}$	parameters defined by eq. (39)
M	coefficient matrix, eq. (25a)
M_∞	free-stream Mach number
m_x, m_y, m_z	intermediate variables defined by eq. (27)
N	coefficient matrix, eq. (25b)
NFLIP	switching parameter defined following eq. (17)
NPHI	number of meridional points (fig. 5)
NT2	number of radial points (fig. 5)
n	index in marching direction
$\vec{n}$	unit normal vector
p	pressure
Q	intermediate variable defined by eq. (27)
q	velocity, $(\sqrt{u^2 + v^2 + w^2})$
R	$= R_w + B^2/R$
R_w	wing semispan in Cartesian space
r_b	body radius in transformed space
r_s	shock radius in transformed space
U	$= (u,v,w,p,\rho)^T$
U,V,W	contravariant velocity components (eq. (5))
(u,v,w)	Cartesian velocity components nondimensionalized by maximum flow velocity
(x,y,z)	Cartesian coordinates

z	$= r \exp i(\phi - \pi/2)$
(z,r,ϕ)	coordinates in transformed space (eq. (3))
α	angle of attack
ρ	density
γ	ratio of specific heats
ϕ	meridional coordinate (fig. 4)
ξ	normalized radial distance, $(r - r_b)/(r_s - r_b)$
μ	damping coefficient, eq. (18)
σ_M	eigenvalues of matrix M
σ_N	eigenvalues of matrix N
$\Delta\theta$	turning angle defined by eq. (34)
∇	gradient operator
Δ	difference operator
θ	$= \phi - \pi/2$
ε	small increment
ψ	wing leading edge sweep angle
(ζ,τ,η)	coordinates in computational space, eq. (7)

Subscripts

r,m	radial, meridional direction
$1,2$	pre and post shock conditions

Superscripts

L,ℓ,jj	dummy parameters defined following eq. (18)
T	transpose operator
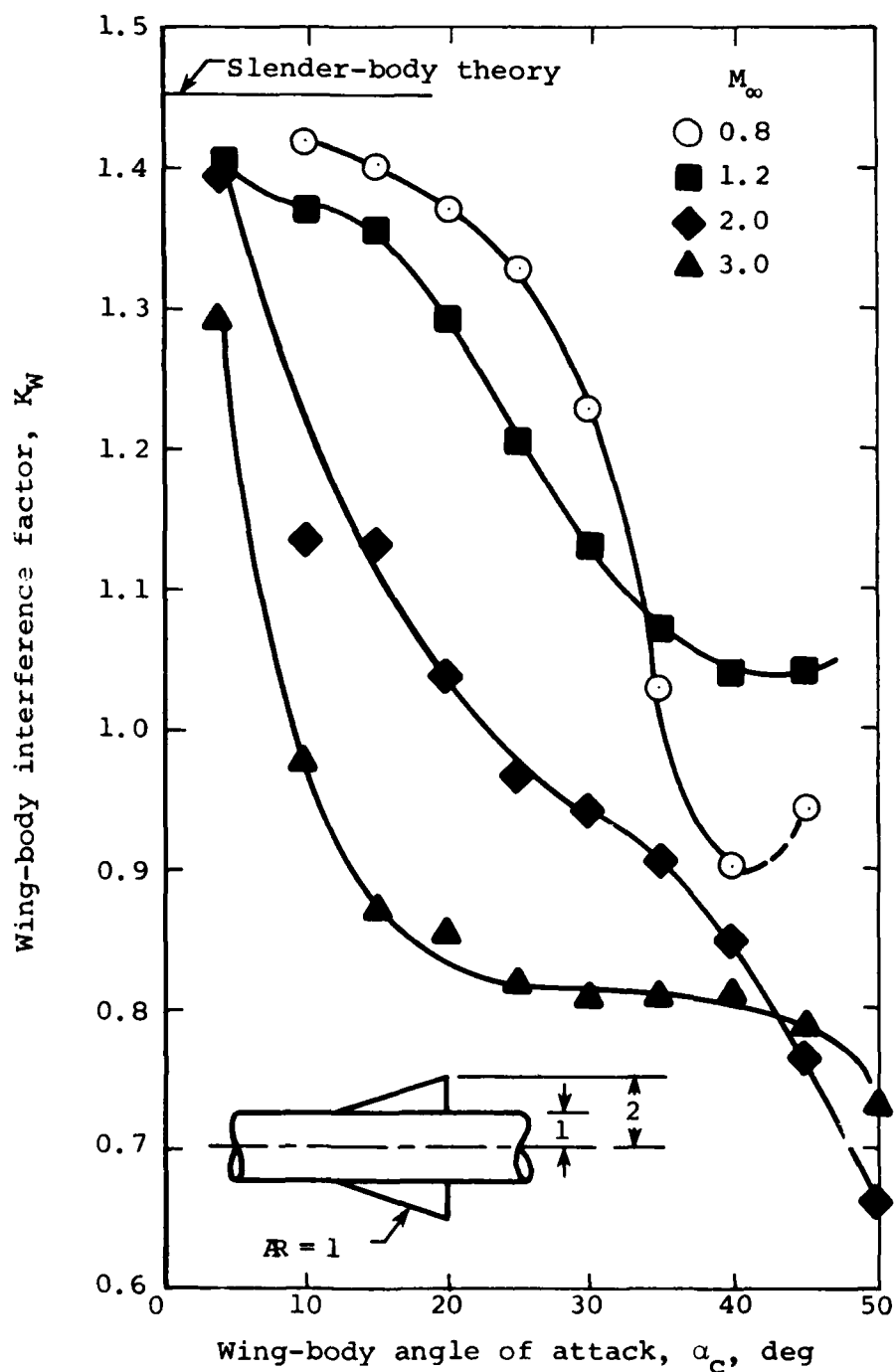
Figure 1.- Effect of angle of attack and free-stream
Mach number on interference of body on wing.

$M_\infty = 2.96$

$\alpha = 28^\circ$

$L = 20$

$D = 3$

$L_n = 9$

Approximate vortical singularity location

A

A

M_∞

z

$M_C = M_\infty \sin \alpha = 1.11$

Bow shock

$M_{c_f} < 1$

Vortical singularity

Crossflow shock

$M_{c_f} > 1$

Sonic line
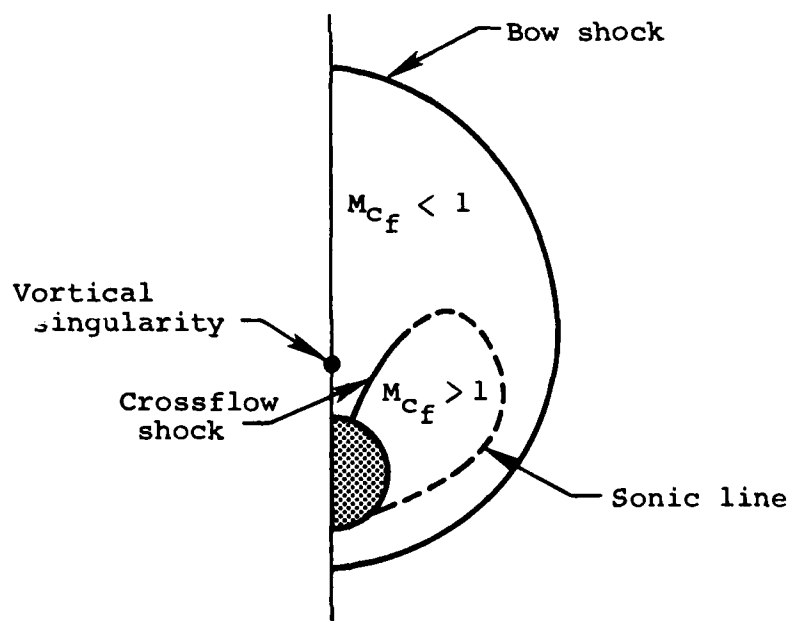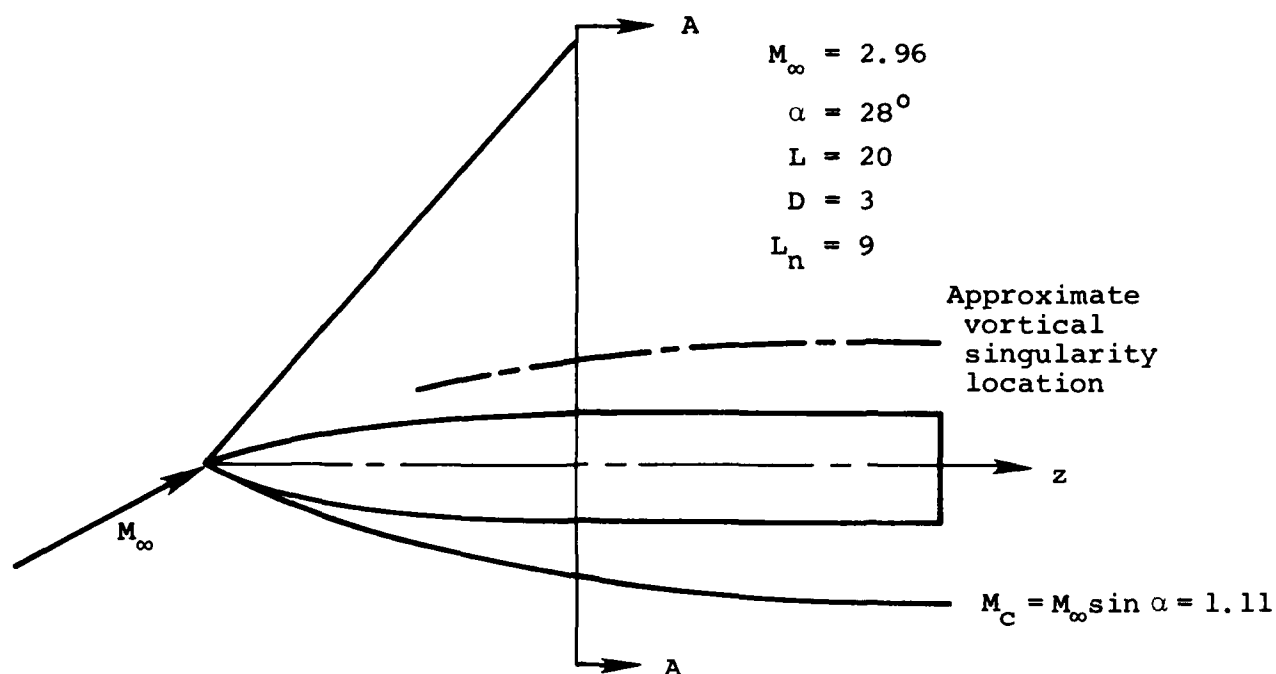
Section A - A

z = 10.04

Figure 2.- Flow in crossflow plane of body of revolution with supersonic crossflow Mach number as obtained from Euler equations.

GRID PLOT

Wing only M_∞ = 3, α = 10, Sweep = 75.964

Wing

y = 0

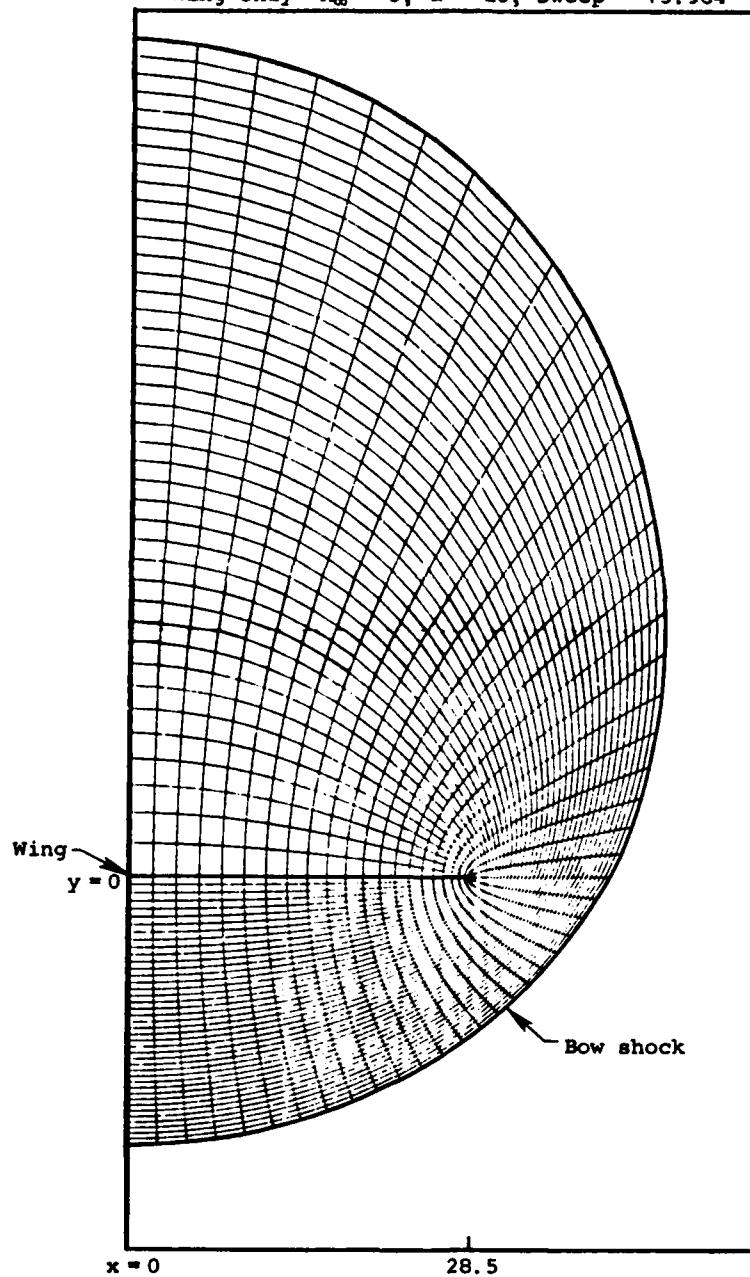Bow shock

x = 0   28.5

Figure 3a.- Mesh for delta wing alone.

64

GRID PLOT

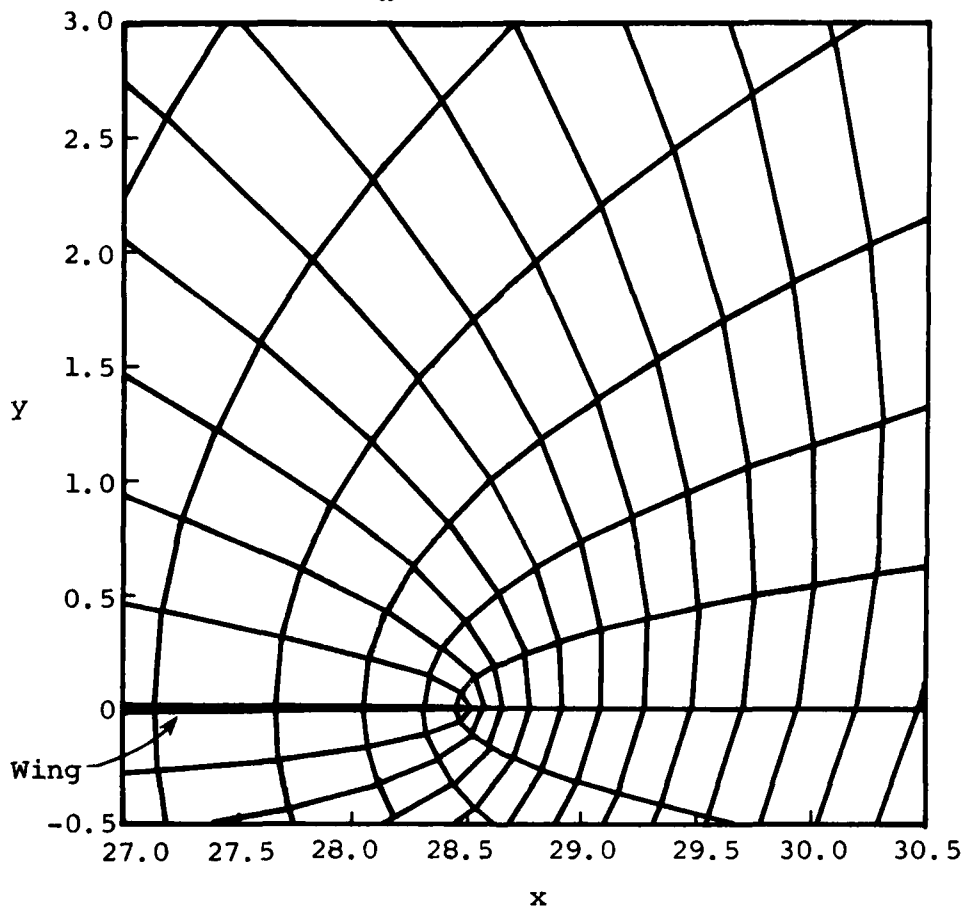Wing only $M_\infty = 3$, $\alpha = 10$, Sweep = 75.964
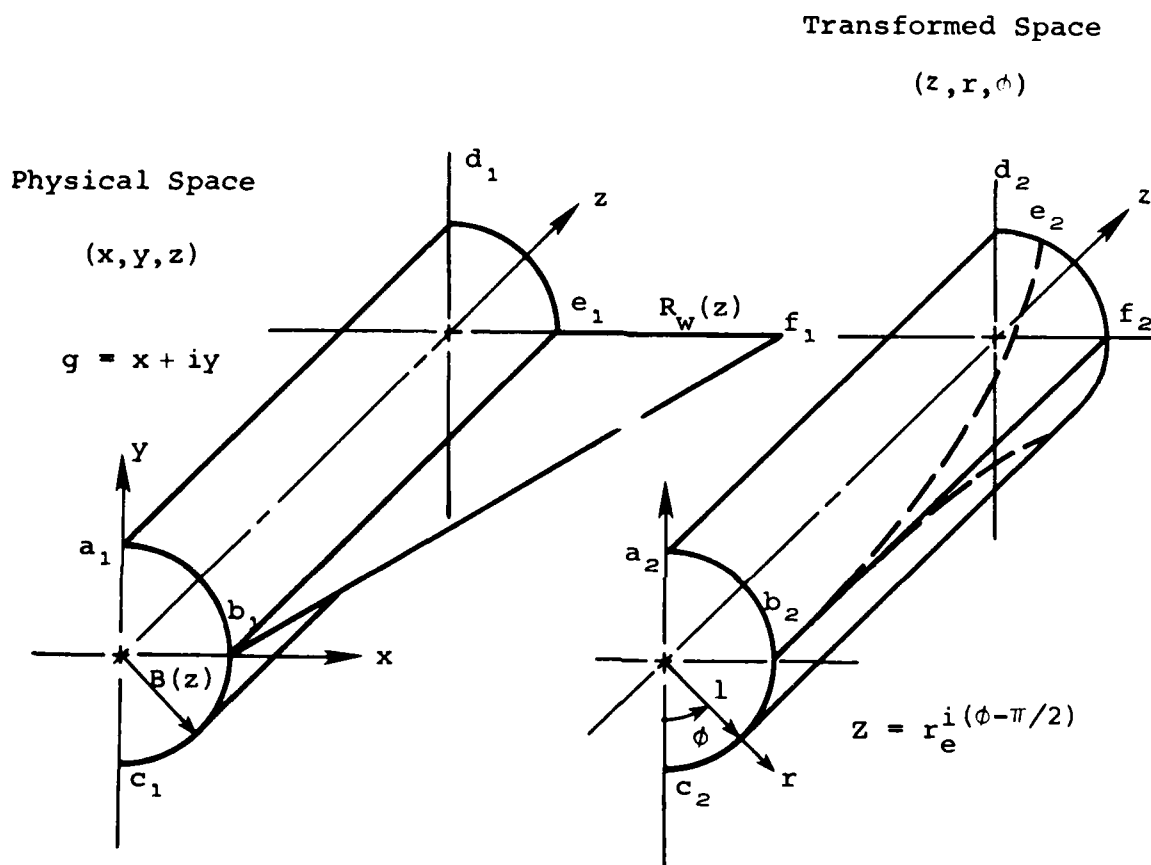

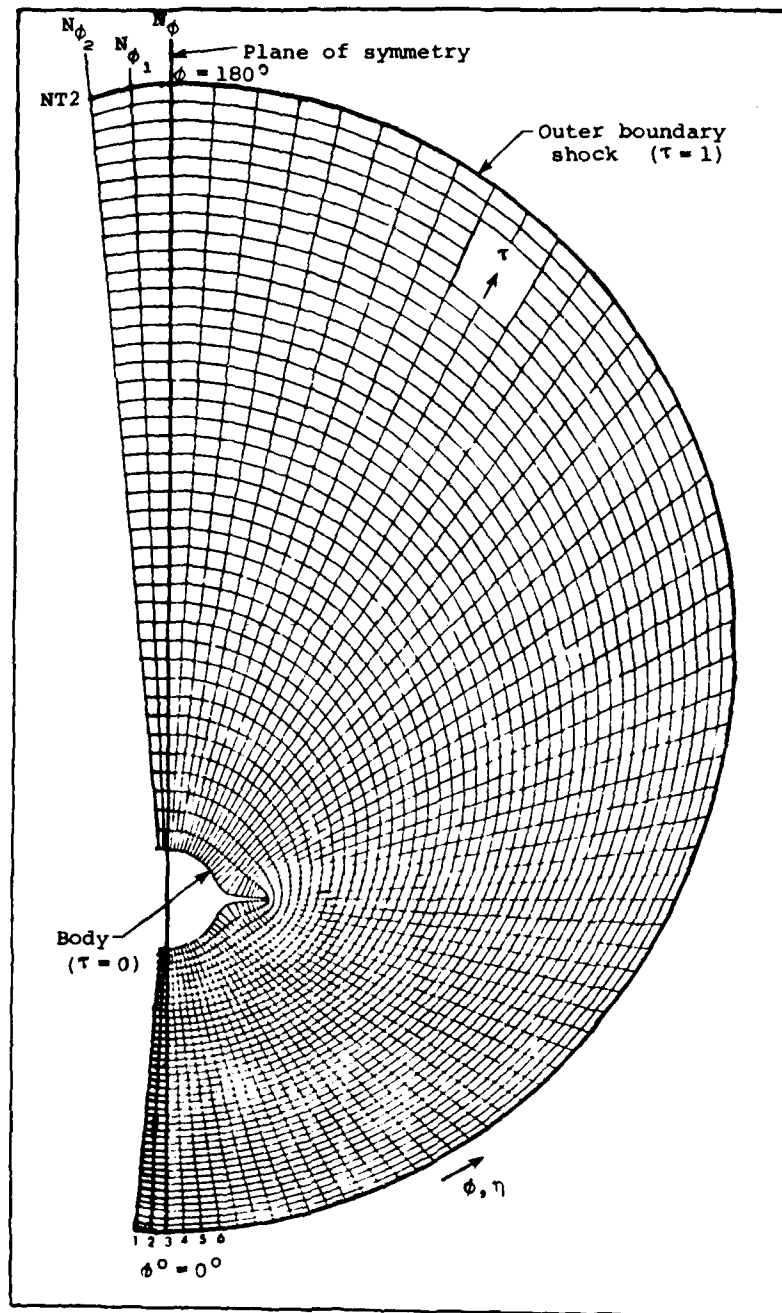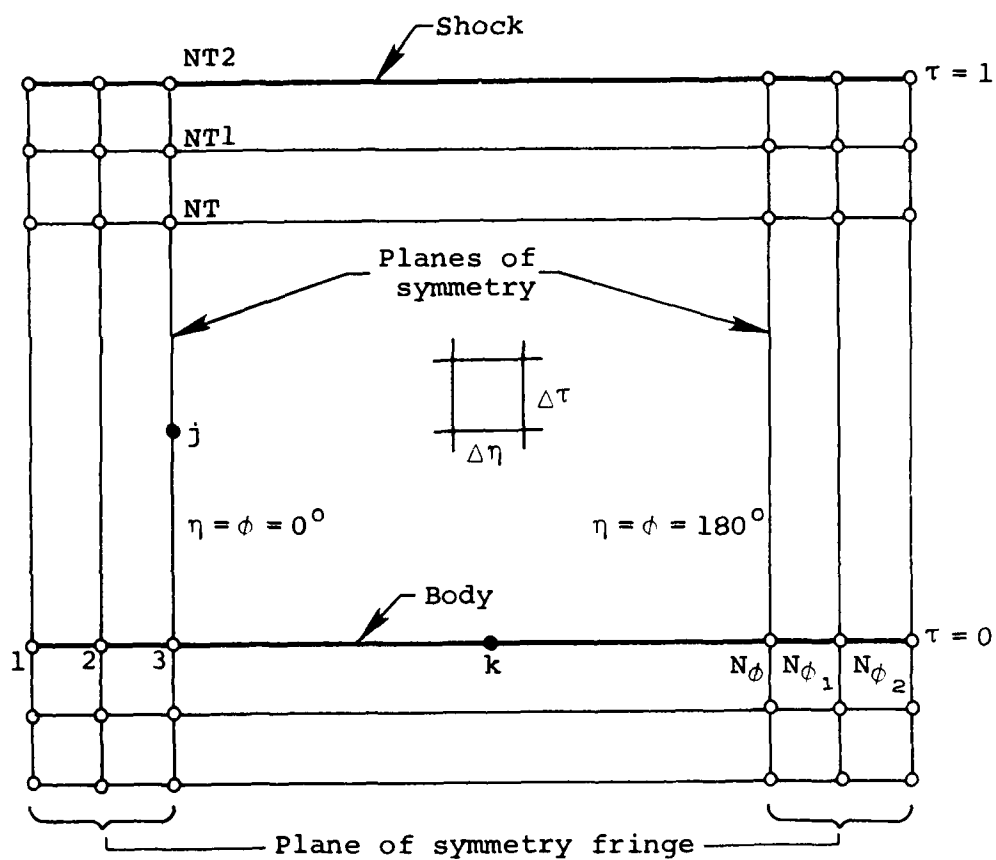Figure 3b.- Detail of mesh near wing leading edge.

Figure 4.- The transformation between the physical space
and the arbitrary curvilinear space.

(a) **Discretized flow region.**

Figure 5.- Mesh description.

67

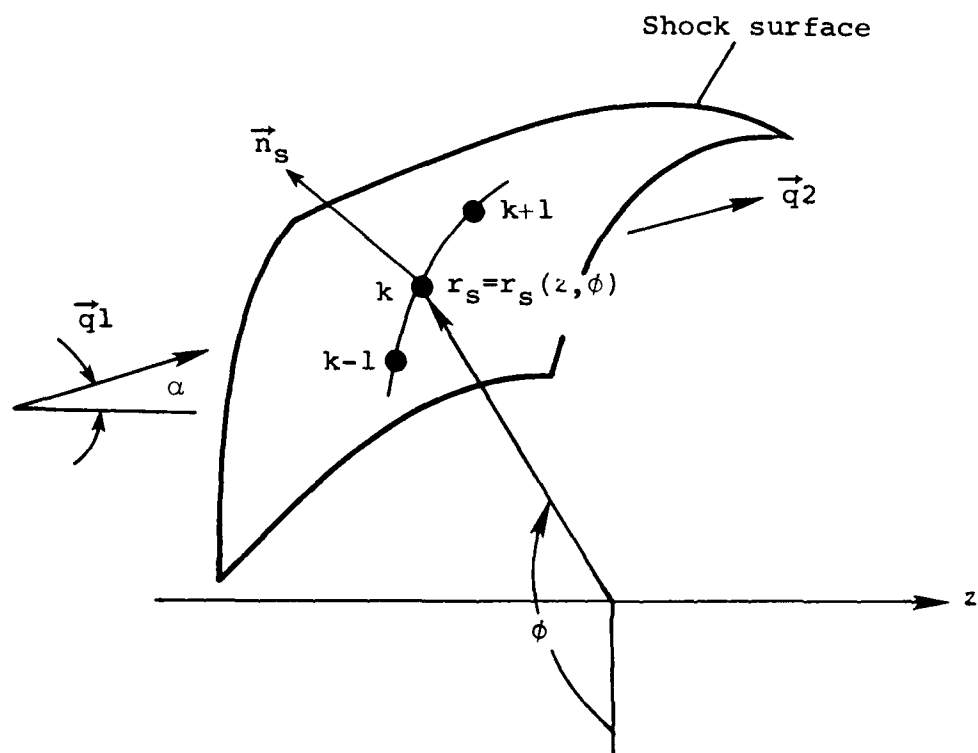(b) Computational plane.
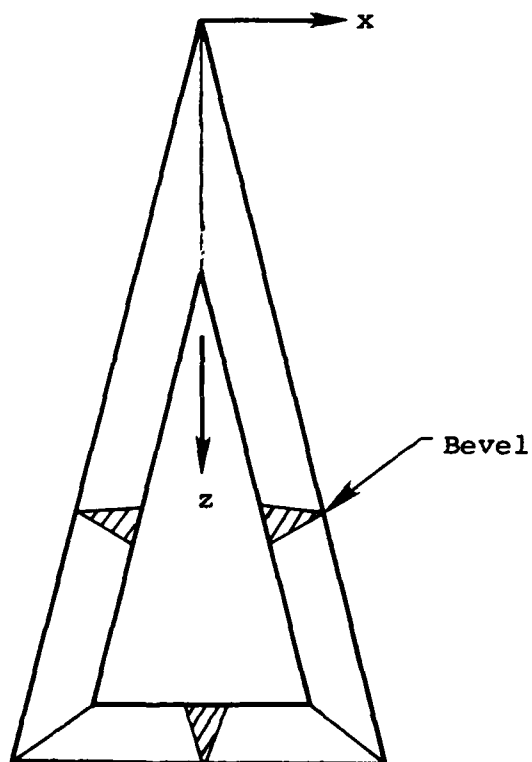
Figure 5.- Continued.

Figure 6.- Steady shock for three-dimensional
supersonic flow in generalized curvilinear
coordinates (z,r,ϕ).

Aspect ratio: 1.0
Thickness: 0.5
Root chord: 12 in
Bevel half angle: 15°

Figure 7a.- Pressure wing geometry.
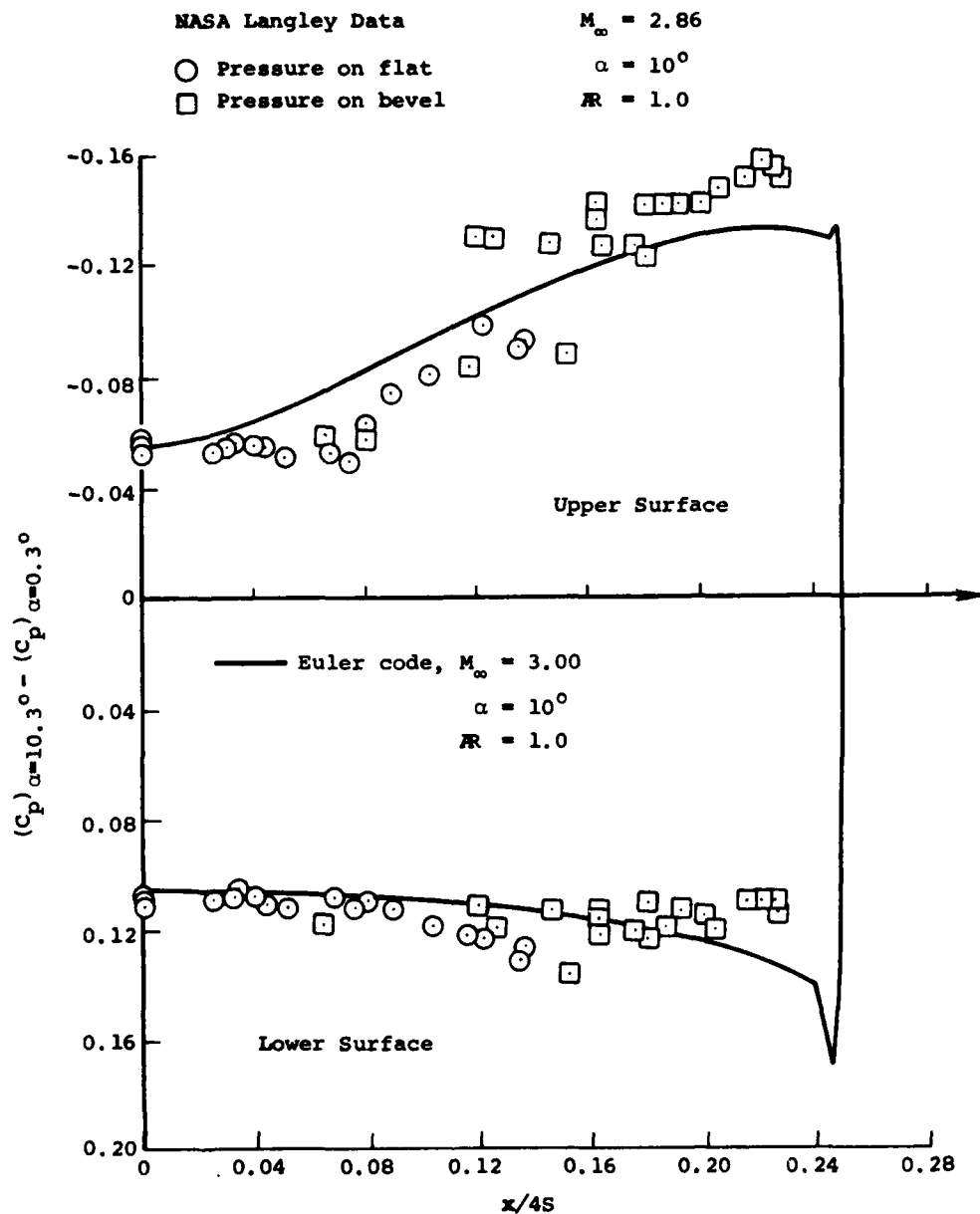
Figure 7b.- Comparison of delta wing pressure distributions
as measured and as calculated using an Euler code
with a Kutta condition.

Angle of attack: 10°

Aspect ratio: 1.0

Mach number: 3.0

2.5

2.0

1.5

y/S

1.0

0.5

0

-0.5

-1.0

0   0.5   1.0   1.5

x/S

Bow shock
wave

Vortical
singularity

Vortical
singularity
(wing root)

Leading edge

Stagnation
stream
surface

Figure 8.- Conical streamlines for delta wing alone
computed by Euler code with Kutta condition.

72

PARTICLE PATHS

Wing only $M_\infty = 3$, $\alpha = 10$, Sweep $= 75.964$

$M_\infty = 3$ $\alpha = 10$ Re $= 0$ Z $= 120$

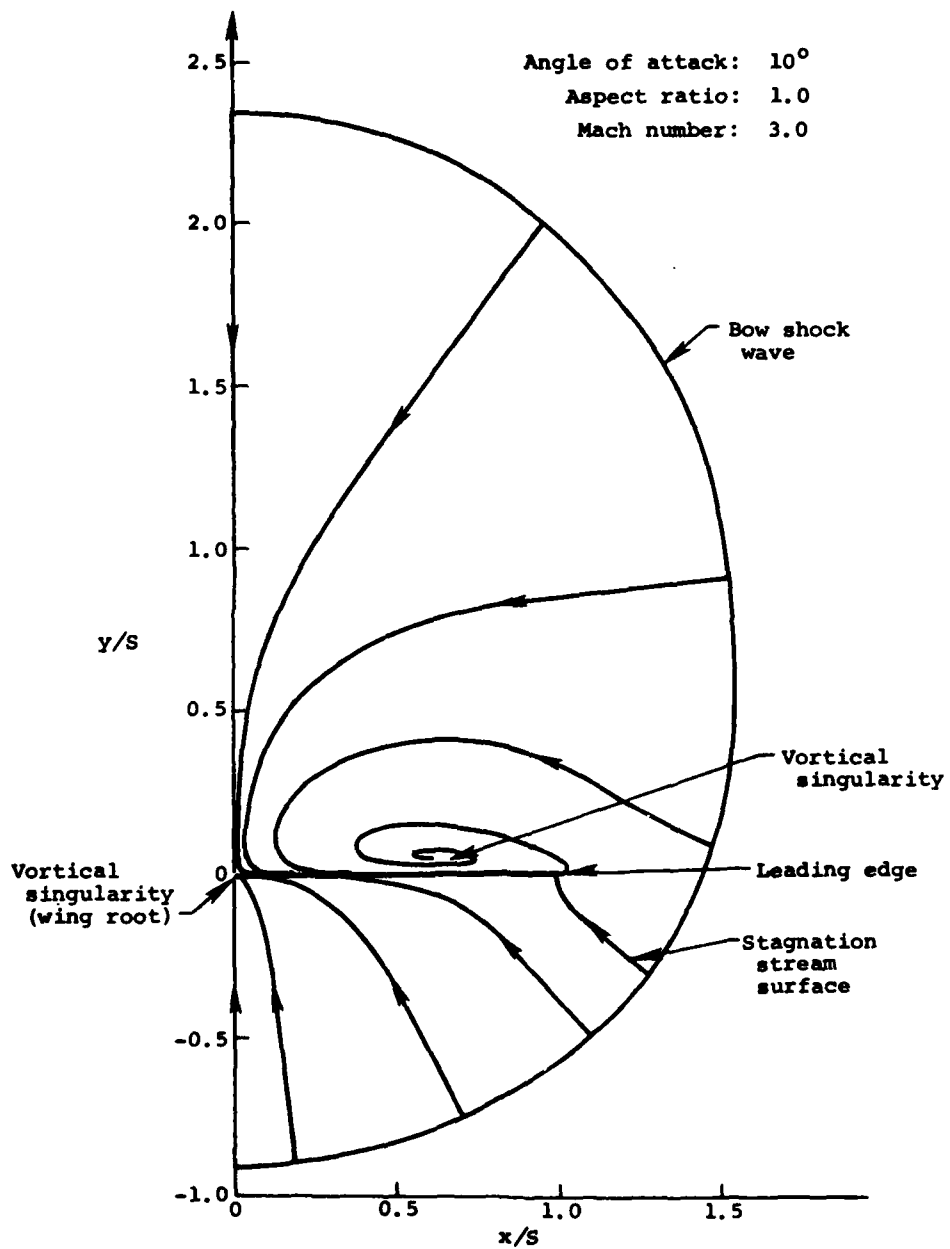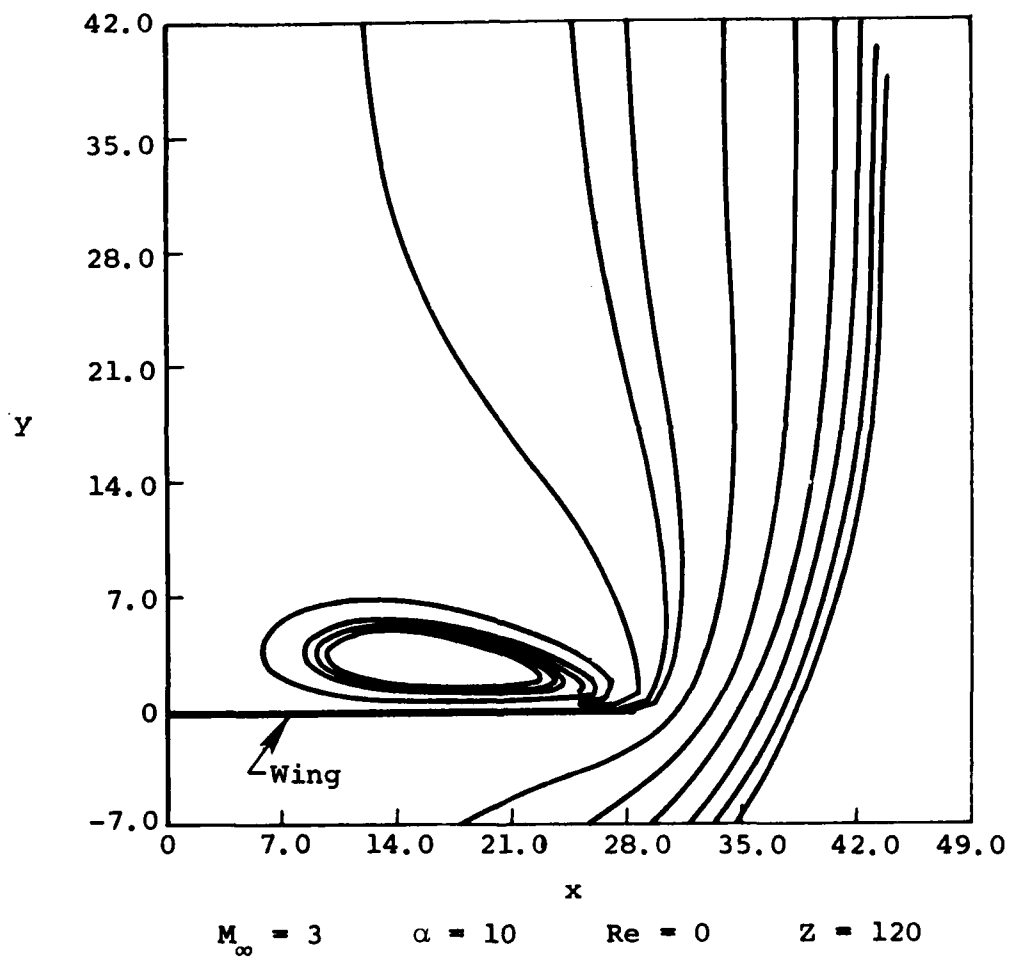Figure 9.- Particle paths obtained by present results
as seen by a vapor screen visualization.

73

VELOCITY VECTORS

Wing only M = 3, α = 10, Sweep = 75.964

y

3.0

2.5

2.0

1.5

1.0

0.5

0

-0.5

27.0   27.5   28.0   28.5   29.0   29.5   30.0   30.5

M_∞ = 3 α = 10   Z = 120   x
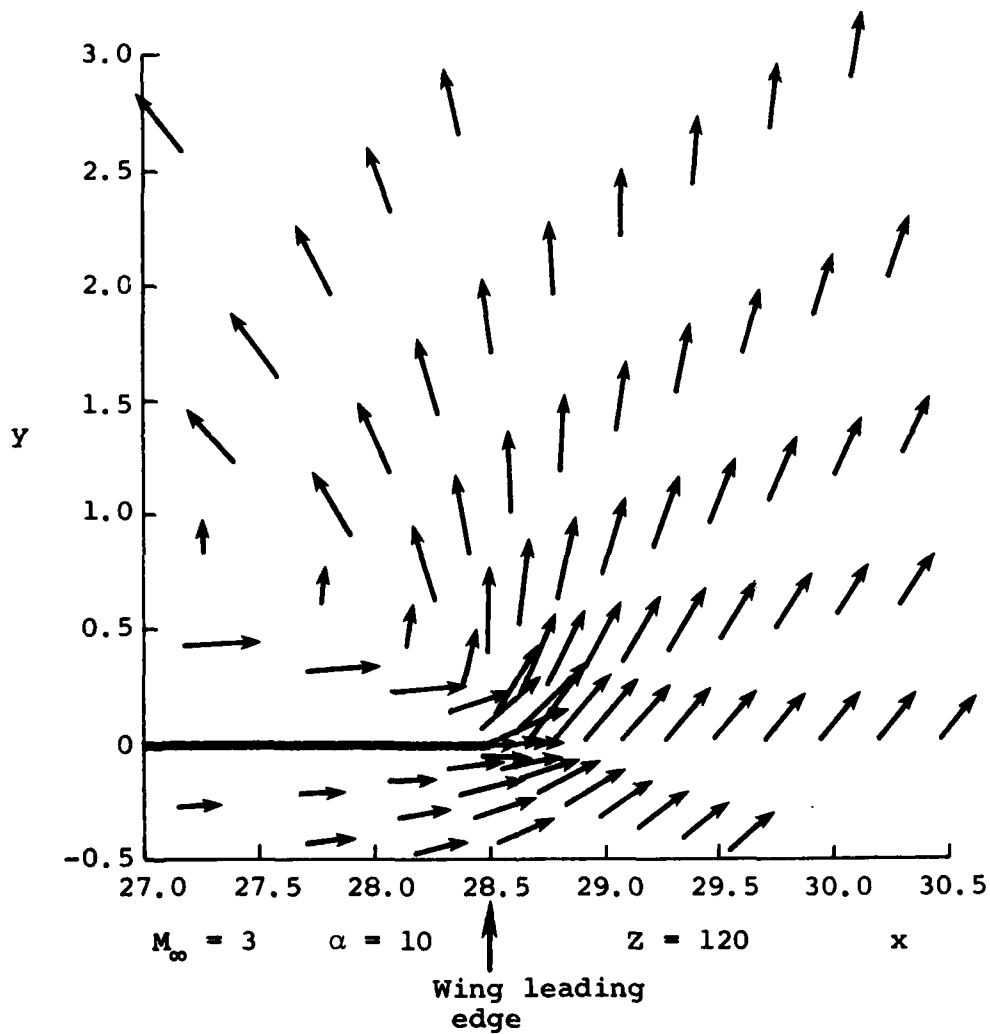
Wing leading
edge

Figure 10.- Cross flow velocity vectors near leading
edge for delta wing alone.

74
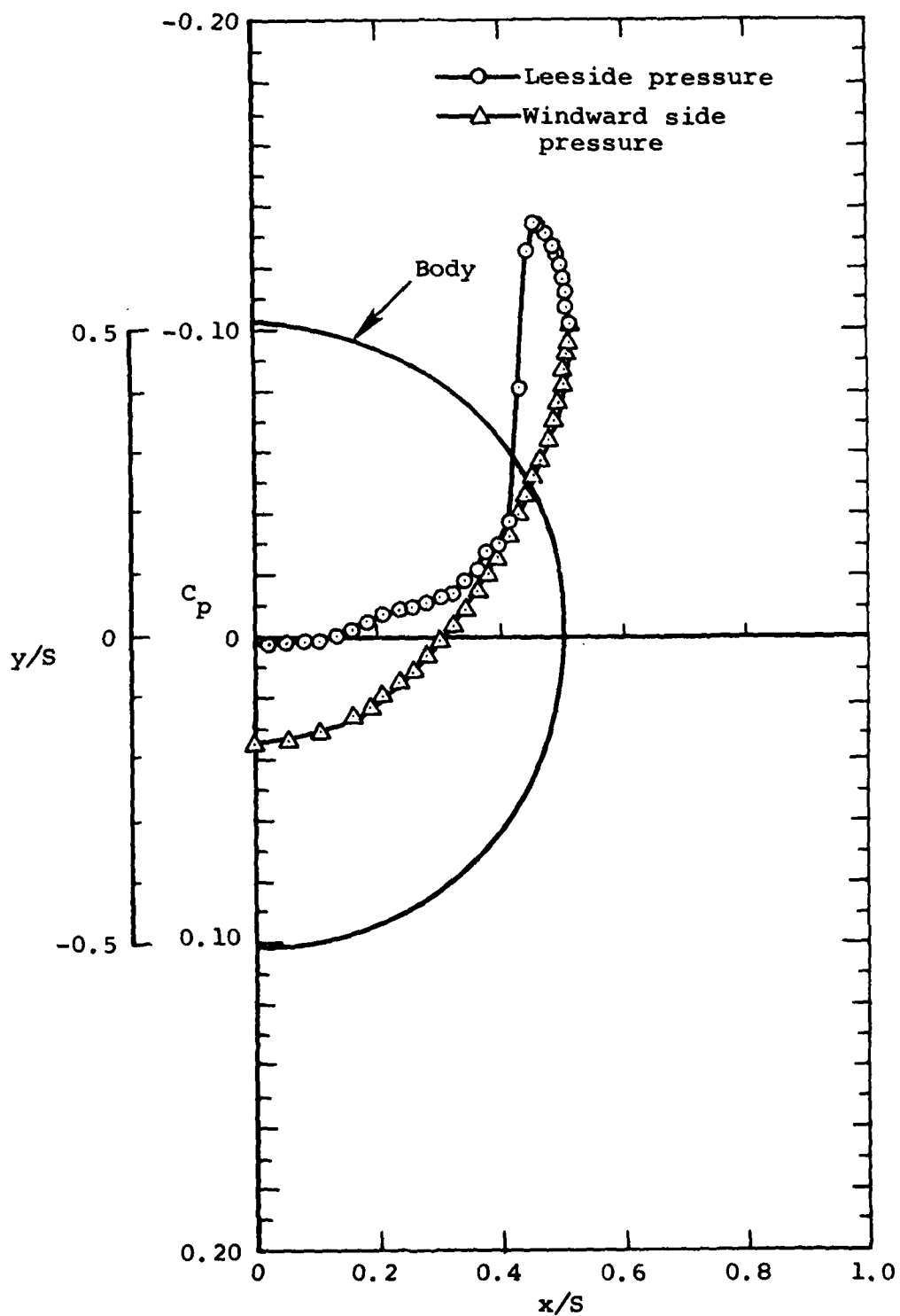
Figure 11a.- Pressure on body at a station just
prior to start of wing.

75

Figure 11b.- Pressure on wing-body at midchord.

Figure 11c.- Pressure on wing-body at the trailing edge.

77

PARTICLE PATHS

Wing body   M = 3,   α = 10,   Sweep = 75.964

Figure 12.- Particle paths of a wing-body configuration
in a crossflow plane at the trailing edge
of the wing.

Figure 13.- Effect of angle of attack and free-stream
Mach number on interference of body on wing.

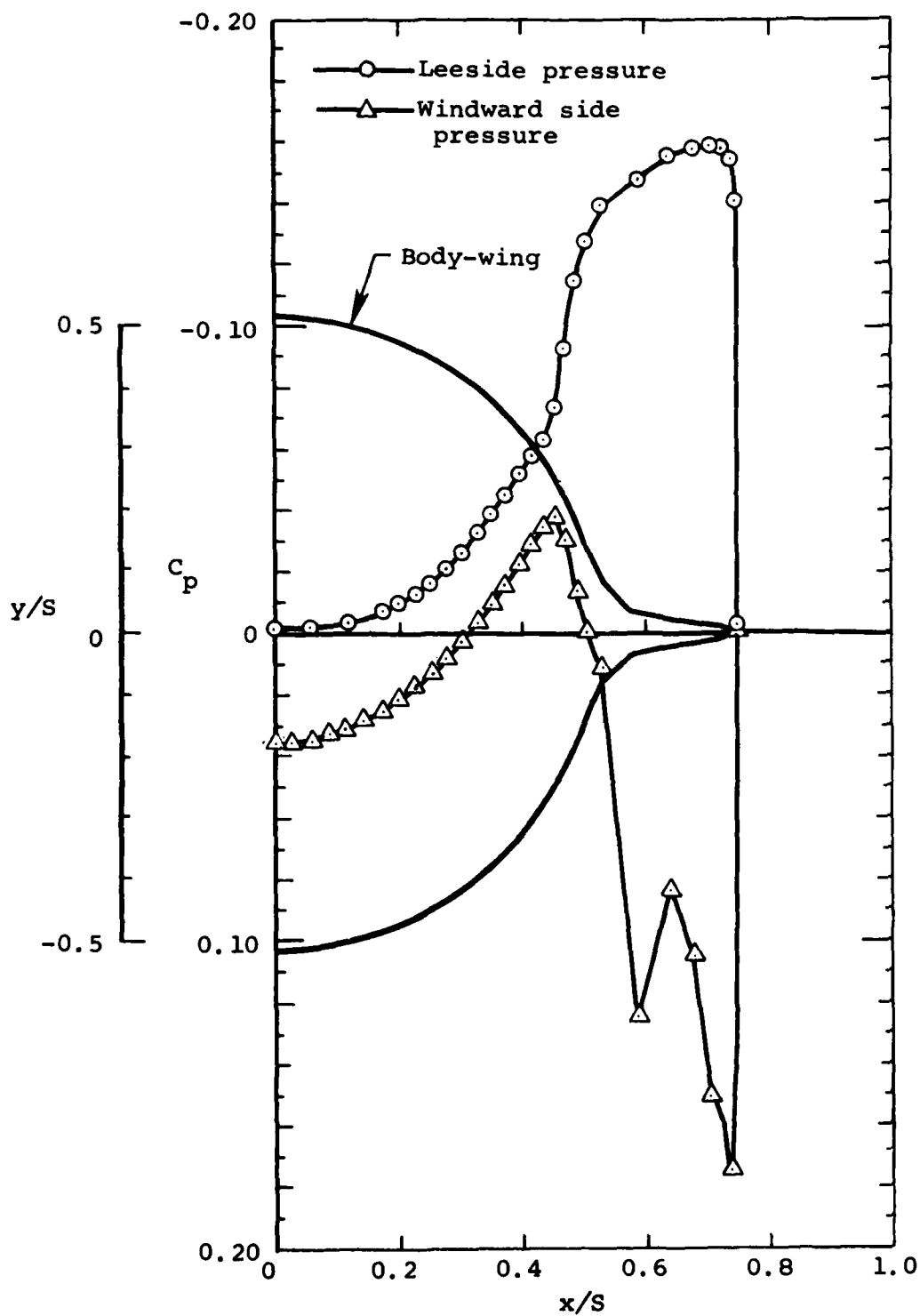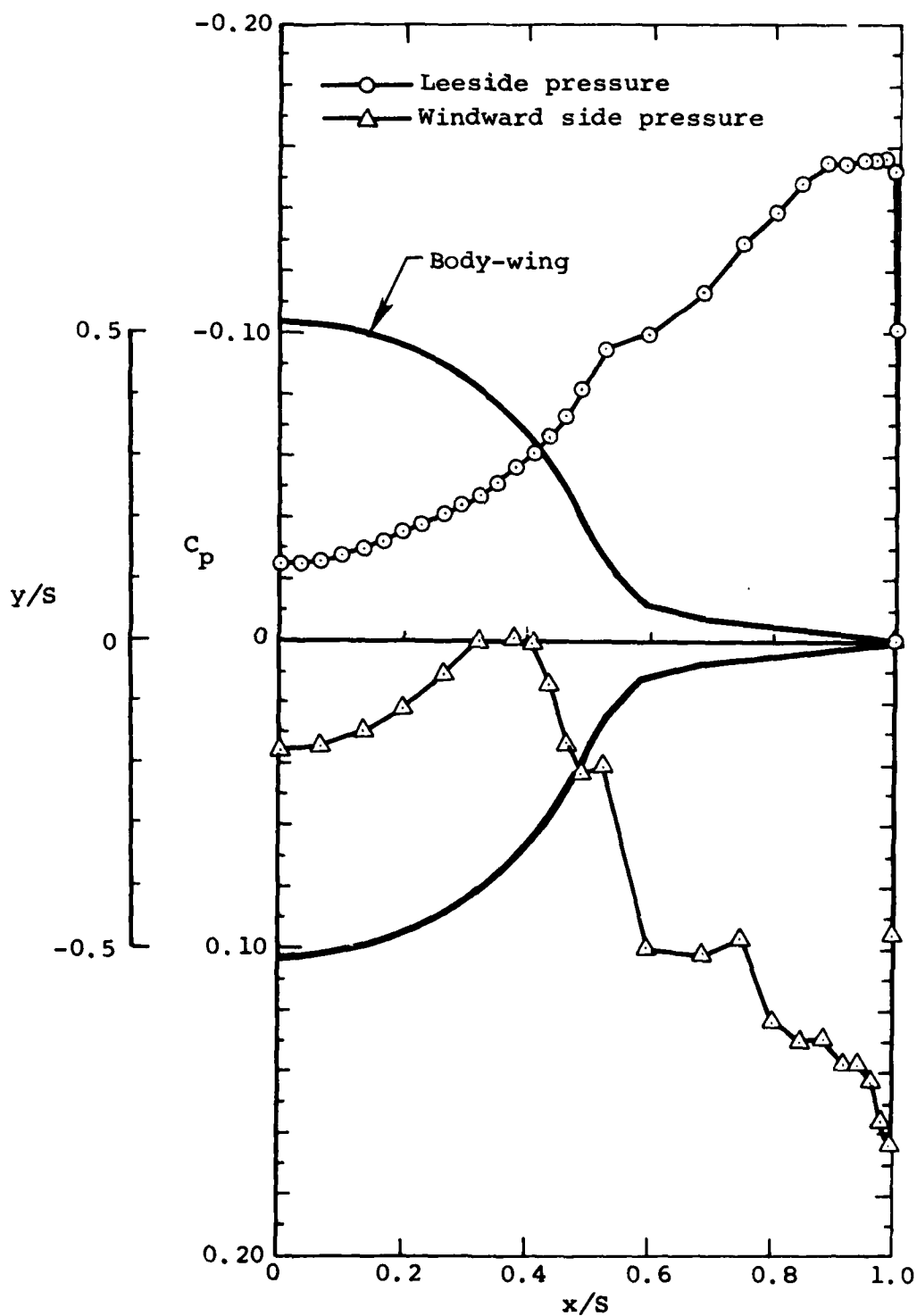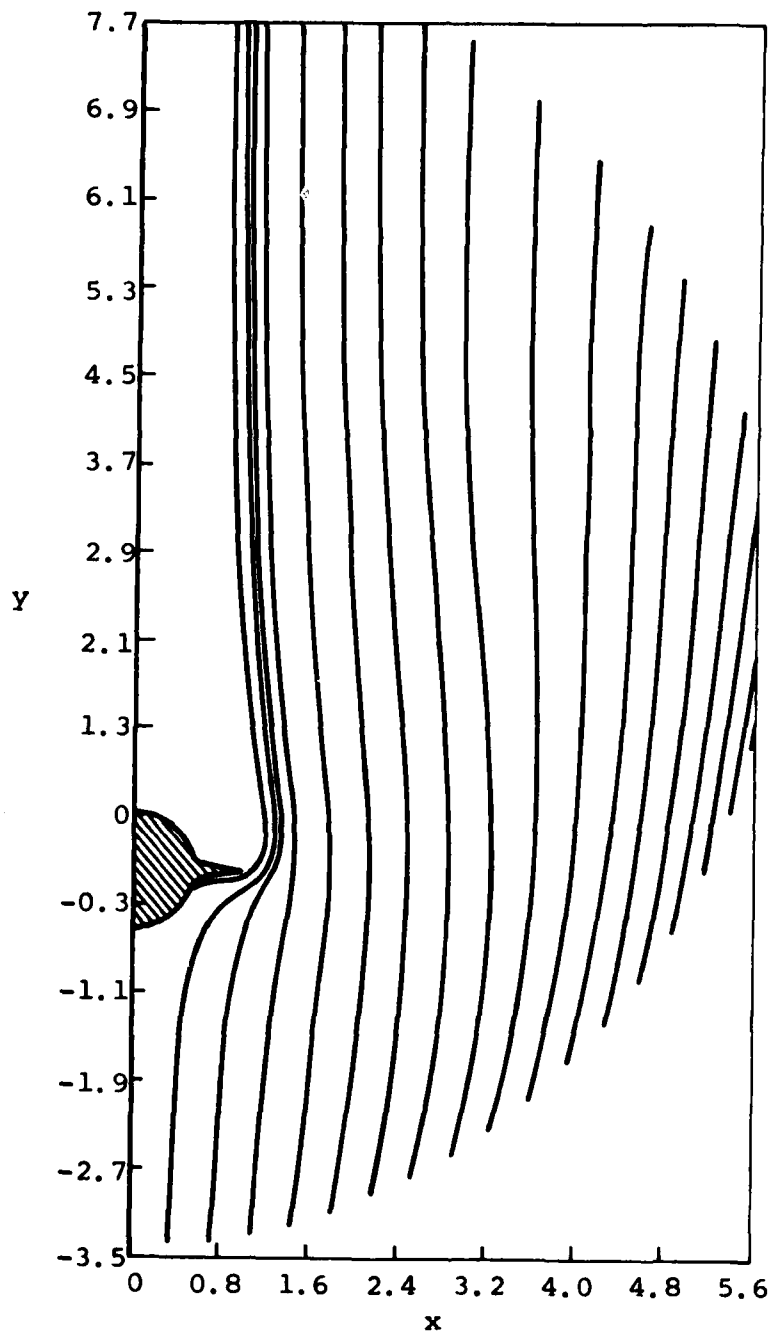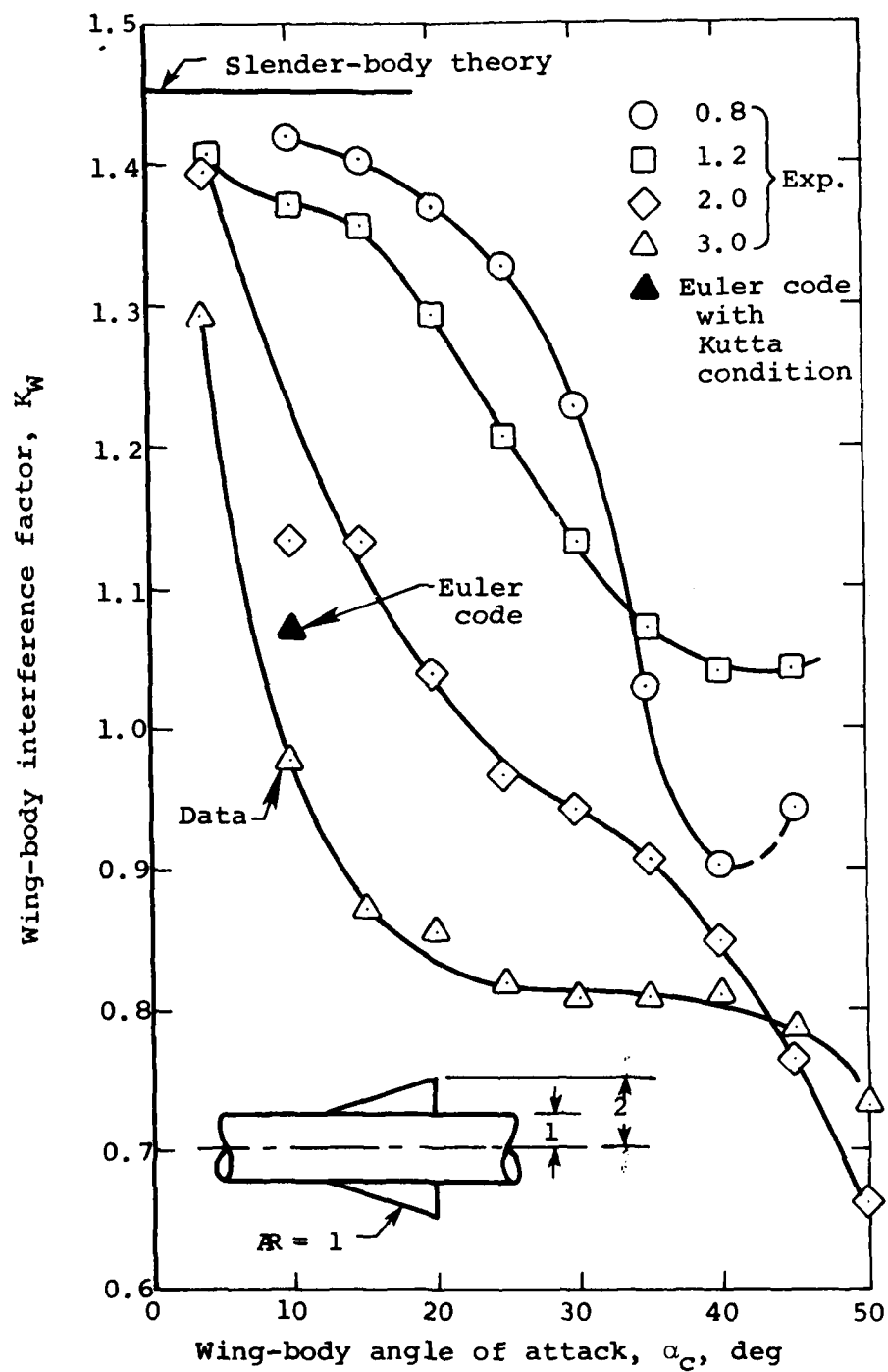|	
Office of Naval Research	Naval Sea Systems Command
800 N. Quincy St.	Washington, DC 20362
Arlington, VA 22217	SEA 0351 (Mr. L. Pasiuk) 1
ONR 211 4	(Dr. T. Peirce) 1
ONR 430B 1	

Office of Naval Research Western
Regional Office (Pasadena)
1030 E. Green St.
Pasadena, CA 91106   1

Defense Contract Admin. Services
Management Area, San Francisco
1250 Bayhill Drive
San Bruno, CA 94066   1

Naval Research Laboratory
Washington, DC 20375
Code 2627   1
Code 2629   1

Defense Technical Information Center
Bldg. 5 Cameron Station
Alexandria, VA 22314   12

Naval Air Systems Command
Washington, DC 20361
AIR 320C (Mr. W. Volz)   1
AIR 320D (Mr. D. Kirkpatrick)   1

Naval Surface Weapons Center
White Oak Laboratory
Silver Spring, MD 20910
Code WA-41 (Mr. F. J. Regan)   2

Naval Surface Weapons Center
Dahlgren Laboratory
Dahlgren, VA 22448
Code DK-21 (Mr. F. L. Stevens)   2
Code DK-21 (Dr. F. Moore)   1

U. S. Naval Postgraduate School
Monterey, CA 93940
Dept. of Aeronautics (Code 57)   1
Library   1

Naval Coastal Systems Laboratory
Panama City, FL 32407
Dr. Neill Smith   1
Dr. D. Humphreys   1

Naval Weapons Center
China Lake, CA 93555
Code 4063 (Mr. S. K. Carter)   1
Code 3914 (Mr. W. H. Clark)   1

Pacific Missile Test Center
Point Mugu, CA 93041
Code 1241 (Mr. K. A. Larsen)   1

David Taylor Naval Ship Research and
Development Center
Bethesda, MD 20084
Code 166 (Mr. J. Nichols)   1
Code 1606 (Dr. S. de los Santos)   1

Naval Air Development Center
Warminster, PA 18974
Code 301 (Mr. J. B. Smith)   1
Code 30P4 (Mr. F. A. Kuster)   1

NASA Langley Research Center
Hampton, VA 23665
Mr. W. C. Sawyer M/S 413   1
Mr. C. M. Jackson M/S 406   1

NASA AMES Research Center
Moffett Field, CA 94035
Dr. G. Chapman   1
Mr. J. Malcolm   1

Wright Patterson Air Force Base
Dayton, OH 45433
AFFDL/FGC (Dr. G. Kurylovich)   1

Eglin Air Force Base
Eglin, FL 32542
AFATL/DLDL (Mr. D. C. Daniel)   1

Arnold Engineering Development Center
Arnold AF Station, TN 37389
AEDC/DYR (Mr. E. R. Thompson)   1

Wright Patterson Air Force Base
Dayton, OH 45433
AFFDL/FGC (Mr. Calvin Dyer)   1

Air Force Office of Scientific
  Research
Bldg. 410
Bolling AFB, DC   20332
  Aerospace Sciences (NA)   1

U. S. Army Missile Command
Redstone Arsenal, AL   35809
  AMSMI-RDK (Mr. R. A. Deep)   1

Sanders Associates Inc.
Nashua, NH   03060
  Mr. J. Smith   1

Hughes Aircraft Corp.
Missile Systems Division
Canoga Park, CA   91304
  Mr. J. B. Harrisberger   1

University of Notre Dame
Aerospace and Mechanical
  Engineering
P. O. Box 537
Notre Dame, IN   46556
  Dr. R. Nelson   1

Honeywell Inc.
600 N. Second St.
Hopkins, NM   55343
  Mr. S. Sopzak   1

Aeronutronics Corp.
Ford Road
Newport Beach, CA   92663
  Mr. R. C. Morenus   1

Raytheon Company
Hartwell Road
Bedford, MA   01730
  Mr. T. Kane   1
  Mr. D. P. Forsmo   1

Johns Hopkins University
Applied Physics Lab.
8621 Georgia Avenue
Silver Spring, MD   20910
  Mr. L. E. Tisserand   1

Rockwell/Missile Systems Div.
4300 East Fifth Avenue
Columbus, OH   43216
  Mr. J. E. Rachner   1

General Dynamics/Pomona
P. O. Box 2507
Pomona, CA   91766
  Mr. F. C. Thomas   1

Martin Marietta
P. O. Box 5837
Orlando, FL   32808
  Mr. G. Aiello   1

McDonnell Douglas Astronautics East
P. O. Box 516
St. Louis, MO   63166
  Mr. J. L. Bledsoe   1

McDonnell Douglas Astronautics West
5301 Bolsa Avenue
Huntington Beach, CA   92647
  Mr. M. Briggs   1
  Mr. Robert Alexander   1
  Dr. James Xerikos   1

Sandia Laboratories
Technical Library
Albuquerque, NM   87115
  Mr. D. Barnette   1

Lockheed Missiles & Space Co., Inc.
Huntsville Research & Engineering Ctr.
P. O. Box 1103
Huntsville, AL   35807
  Mr. A. Zalay   1

McDonnell Douglas Astronautics West
5301 Bolsa Avenue
Huntington Beach, CA   92647
  Mr. K. Kiser   1

University of Texas
Austin, TX   78712
  Dr. William L. Oberkampf   1

ARO Inc.
PWT/4T
Arnold AFS, TN   37389
  Dr. T. Hsieh   1

Aberdeen Proving Ground
Ballistics Research Laboratory
Aberdeen, MD   20015
  Dr. Charlie H. Murphy   1

Applied Sciences Division
Large Caliber Laboratory
Picatinny Arsenal, NJ   07801
  Mr. Alfred A. Loeb   1

AEDC/DOTR
Arnold AFS, TN   37389
  A. F. Money   1

Aeroballistics Directorate
U. S. Army Missile Research
  Development & Engineering
  Laboratory
U. S. Army Missile Command
Redstone Arsenal, AL   35809
  DRSMI-RDK (Dr. D. J. Spring)   1

Lockheed Missile & Space Co.
P. O. Box 504
Sunnyvale, CA   94088
  Dept. 81-10, Bldg. 154,
    (Dr. Lars/E. Ericsson)   1

NASA Langley Research Center
Hampton, VA   23665
  Miss Emma Jean Landrum, M/S 402   1

ARO, Inc.
PWT/4T
Arnold AFS, TN   37389
  Dr. William B. Baker, Jr.   1

DATE FILMED

9-8